

Revealing kinetically tuned atomic pathways for interfacial strain relaxation

Sophia B. Betzler,^{1, †} Daewon Lee,^{1, 2, †} Sam Oaks-Leaf,^{3, †} Colin Ophus,⁴ Lin-Wang Wang,⁵ Mark Asta,^{1, 2} David T. Limmer^{*, 1, 3, 6, 7, a)} and Haimei Zheng^{*1, 2, b)}

¹⁾ *Materials Sciences Division, Lawrence Berkeley National Laboratory; Berkeley, CA, USA*

²⁾ *Department of Materials Science and Engineering, University of California, Berkeley, CA, USA*

³⁾ *Department of Chemistry, University of California, Berkeley; Berkeley, CA, USA*

⁴⁾ *National Center for Electron Microscopy, Molecular Foundry, Lawrence Berkeley National Laboratory; Berkeley, CA, USA*

⁵⁾ *State Key Laboratory of Superlattices and Microstructures, Institute of Semiconductors, Chinese Academy of Science; Beijing, China*

⁶⁾ *Chemical Sciences Division, Lawrence Berkeley National Laboratory; Berkeley, CA, USA*

⁷⁾ *Kavli Energy Nanoscience Institute; Berkeley, CA, USA*

(Dated: 10 April 2024)

Strain at interfaces may profoundly impact the microstructure and properties of materials; thus, it is a major consideration when designing and engineering materials.^{1–8} Dislocation formation is a commonly known mechanism to release mismatch strain at solid-solid interfaces. However, it is still unclear about how materials accommodate interfacial strain under drastically accelerated structural transformation kinetics, since it is extremely challenging to directly observe the atomic structure evolution of fast-propagating interfaces. Utilizing liquid phase transmission electron microscopy (TEM), we have achieved atomic-scale imaging of hydrogen-induced phase transformations of palladium nanocrystals with different transformation speeds. Our observation reveals that the fast phase transformation occurs with an expanded interface of mixed α - and β -PdH_x phases, and tilting of (020) planes to accommodate mismatch strain. In contrast, slow phase transformations lead to sharp interfaces with slipping misfit dislocations. Our kinetic Monte Carlo simulations show that fast phase transformation pushes the system far-from-equilibrium, generically roughening the interface; however, a smooth boundary minimizes strain near-equilibrium. Unveiling the atomic pathways of transformations from near-equilibrium to far-from-equilibrium, which was previously possible only computationally, this work holds significant implications for engineering microstructure of materials through modulating solid-solid transformations in a wide range of kinetics.

Introduction

Understanding structural modifications at interfaces by mismatch strain during growth or structural transformations of materials has been a long-standing significant topic of study.^{9–12} Compared to the spectroscopic or computational approaches, *in situ* transmission electron microscopy (TEM) allows us to directly observe spatially resolved atomic structure evolution coupled with the strain relaxation at interfaces during dynamic transformations. For example, the recent work² on imaging of dislocation movements along Cu₂O/Cu interfaces during the reduction reaction of Cu₂O to Cu in H₂ marked the technical advances in observing dynamic dislocation motion under complex environmental stimuli beyond deformation.¹³ However, due to technical challenges in varying the kinetics of structural transformations over a wide range while observing the respective atomic structure evolution, it has not been possible to extend our understanding of the mismatch strain relaxation mechanisms beyond dislocation formation. Specifically, we have not been able to uncover alternative actual routes to accommodate mismatch strain at solid-solid interfaces in

the nonequilibrium regime that are relevant to the practical engineering of materials.

Here, utilizing high-resolution liquid phase TEM, we track the atomic structural evolution of hydrogen-induced phase transformations in palladium (Pd) nanocrystals, which has enabled breakthroughs in revealing mismatch strain relaxation mechanisms at interfaces tuned by phase transformation kinetics. The electron beam radiolysis of water generates hydrogen gases inside a liquid cell. By controlling the amount of hydrogen in the cell, we can modulate the phase transformation kinetics. Two immiscible phases can be obtained when hydrogen is absorbed into Pd, which are α -PdH_x ($x < 0.03$) and β -PdH_x ($x > 0.6$), with a large lattice mismatch by 3.5% between them.^{14,15} Thus, hydrogen absorption and desorption in a palladium nanocrystal generate lattice mismatch strain at the interfaces between α - and β -PdH_x. Hydrogen desorption is a reverse process of hydrogen absorption, providing an additional degree of freedom in tuning the phase transformation kinetics. Despite significant prior efforts in investigating hydrogen sorption behaviors of Pd nanoparticles^{4,6,16–27} *in situ* atomic-scale imaging of hydrogen-induced phase transformations in Pd nanocrystals has not been achieved. Our unprecedented capability allows us to capture the atomic structure evolution at interfaces and reveal distinct mismatch strain relaxation mechanisms under drastically different phase transformation kinetics.

[†]These authors contributed equally to this work.

^{a)} Electronic mail: dlimmer@berkeley.edu

^{b)} Electronic mail: hmzheng@lbl.gov

Disparate phase transformation kinetics

Fig. 1a illustrates the experimental setup for liquid phase TEM study of hydrogen-induced phase transformations in Pd nanocrystals. The Pd nanocubes (40-50 nm) are synthesized following the published synthesis protocol²⁵ (see **Methods**). Representative high-resolution TEM (HRTEM), bright-field TEM, and scanning TEM images of a Pd nanocube are displayed in **Fig. 1b** and **Supplementary Figs. 1 and 2**. A droplet of Pd nanocubes in 0.1 M KOH aqueous solution is loaded into a liquid cell, and small liquid pockets are formed inside the liquid cell^{28,29} (see **Methods** and **Supplementary Fig. 3**). Radiolysis of water yields many products, including the predominant hydrogen and oxygen gases (molar ratio of hydrogen:oxygen estimated to be 60:40).^{30–32} By controlling the dose rate used during TEM experiments, we can control the amount of hydrogen in the liquid cell and thus the transformation kinetics including the phase propagation pathways and propagation rate (see **Methods** and **Supplementary Figs. 4 and 5**).

During hydrogen absorption in a Pd nanocube, the β -PdH_x phase nucleates at a corner, and it subsequently propagates along the [100] direction (see **Methods**, **Supplementary Note 1**, **Supplementary Figs. 6 and 7**, **Supplementary Video 1**, and **Extended Data Fig. 1**). This is consistent with the previously reported phase transformation pathway.^{22–25} To understand the basic thermodynamic driving forces underpinning the observed transformation pathway, we establish a minimal model to simulate the nanoscale dynamics of solid-solid phase transformations. We first calculate both the energetic and the free energetic cost of forming interfacial structures within our model (see **Supplementary Notes 2 and 3**, **Supplementary Figs. 8 and 9**, and **Supplementary Tables 1 and 2**). Our simulations using an elastic Ising model Hamiltonian^{33–35} indicate that the pathway of corner nucleation followed by propagation along the [100] direction during hydrogen absorption can be understood predominantly in terms of the energetics of elastic interactions (see **Extended Data Figs. 2 and 3**, **Supplementary Note 4**, and **Supplementary Video 2**). The reversible transformations of hydrogen absorption and desorption in Pd nanocrystals can be understood by the same set of elastic interaction terms.

To understand the effects of phase propagation rates on the interface structures, we focus on the simple configurations of phase transformations with the interfaces propagating along the [100] directions. We measure the rates of phase propagation along the [100] directions during both hydrogen absorption and desorption in Pd nanocrystals. Dramatically different phase propagation rates are found in the hydrogen absorption and desorption. Representative sequential HRTEM images and the corresponding *d*-spacing phase maps show the phase propagation in both scenarios (**Fig. 1c,d** and **Supplementary Videos 3 and 4**). The phase propagation rates, estimated by the interface position relative to the starting position as a function of time, are illustrated in **Fig. 1e** and **Supple-**

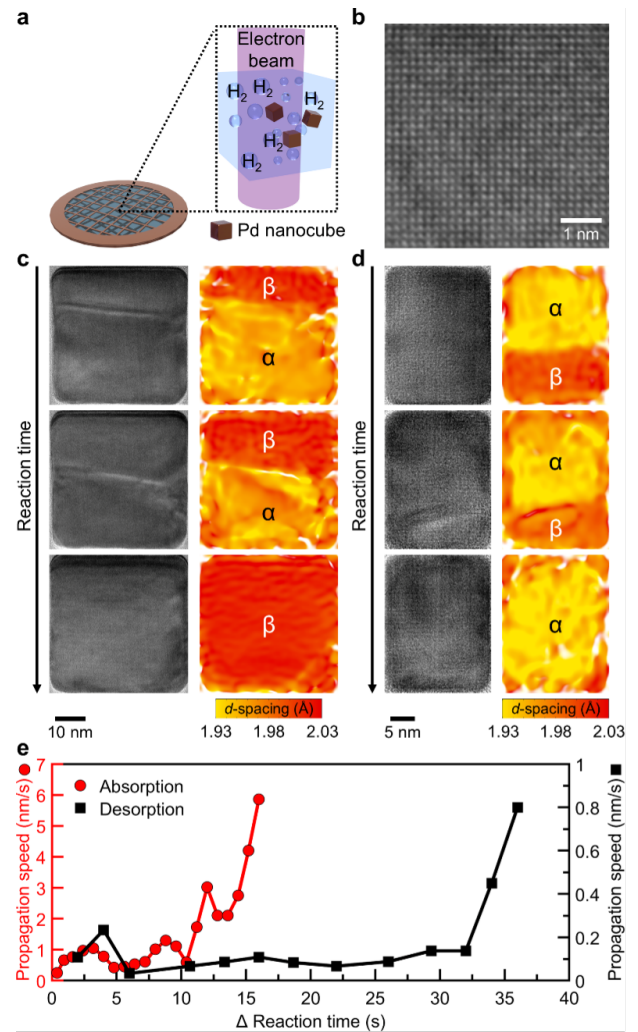


FIG. 1: *In situ* liquid phase TEM study of hydrogen absorption and desorption in Pd nanocubes. **a**, Schematic illustration of the experimental setup. The electron beam radiolysis of water generates hydrogen gases in the liquid cell, and the hydrogen sorption behaviors in Pd nanocubes are observed in real-time with atomic resolution. **b**, An HRTEM image of Pd nanocube showing single-crystal structure. **c,d**, Sequential HRTEM images and corresponding *d*-spacing color maps of Pd nanocubes during hydrogen absorption (**c**) and desorption (**d**), leading to the β -PdH_x and α -PdH_x phases, respectively. **e**, The average propagation speed of the interface along the [100] direction as a function of time during hydrogen absorption (left *y*-axis) and desorption (right *y*-axis). The propagation speed of hydrogen absorption is about one order magnitude faster than the desorption. Details about the interface position measurements and methods to derive the average propagation speed are described in **Supplementary Figs. 10 and 11**.

mentary Figs. 10 and 11.

During hydrogen absorption (Fig. 1e, left y -axis and Supplementary Figs. 10a and 11a), the interface propagates along the [100] direction with an average speed of 1.3 nm/s at the early stage. When roughly 50% of the nanocube is transformed, the average propagation speed increases to 3.0 nm/s. The interphase boundary propagates rapidly in the later stages with the average propagation speed of 5.9 nm/s. And, the movement of the interface is not perfectly parallel to the edge of the nanocrystal, with the propagating interface on the left side slower than the right side, which might be attributed to the variations of strain along different crystallographic directions.²³ During the desorption (Fig. 1e, right y -axis and Supplementary Figs. 10b and 11b), a significantly slower propagation speed of 0.2 nm/s is obtained. Similar to the hydrogen absorption, phase propagation occurs rapidly at the last stages of the desorption, with the measured average speed of 0.8 nm/s. Our kinetic model predicts that both absorption and desorption are fastest at the corners of the nanocubes, which could lead to an increase in propagation speed at the end as the interface nears the cube surface. We confirm the completion of phase transformations into α -PdH_x after the desorption or β -PdH_x after the absorption by measuring lattice d -spacings (Supplementary Figs. 12 and 13). The final nanocubes are perfect single crystals without noticeable defects. Moreover, we have observed the swelling or shrinking of the nanocubes due to the uptake or release of hydrogen (Supplementary Figs. 14 and 15). The differences of one order of magnitude in phase propagation rates may arise from the additional kinetic barrier to form hydrogen bonds when hydrogen comes out from Pd nanocrystals during hydrogen desorption.²⁶

A unique expanded interface in fast kinetics

To examine the atomic structure evolution of the interfaces during hydrogen absorption, we analyze a selected representative HRTEM image (from Supplementary Video 3) to elucidate the atomic arrangements (Fig. 2a). The presence of two crystal phases is reflected in the splitting of {200} and {220} diffraction spots in the fast Fourier transformation (FFT) pattern (Fig. 2a inset and Supplementary Fig. 16), and it can also be visualized by tracking the d -spacing within the nanocube (Fig. 2b and Supplementary Fig. 16). A spatially expanded interface is found as illustrated in Fig. 2c, where the last atomic columns without obvious displacements in both α -PdH_x and the newly formed β -PdH_x are highlighted. We employ geometric phase analysis (GPA)^{36,37} to analyze the lattice mismatch strain. We analyze the strain in both [010] (E_{xx}) and [100] (E_{yy}) directions. An overlay of the E_{yy} strain map and the corresponding high-resolution image is displayed in Fig. 2d. It is well known that it is challenging to obtain the quantitative GPA results at interfaces,³⁸ which is reflected by the significantly wide range of strain values in Fig. 2d. More careful investigation of the d -spacing values in the real space is

carried out in Fig. 2e. The E_{yy} GPA strain map qualitatively demonstrates large variations of d -spacing at the expanded interface. Relatively smooth strain variations are observed at the interface in the E_{xx} direction (Supplementary Fig. 17). We examine the highlighted area shown in Fig. 2c, and no edge dislocations can be identified. Dislocations are found within the expanded interface outside the field of view. These illustrate more complex interphase boundary structures during hydrogen absorption with the rapid phase propagation kinetics.

We further calculate the d -spacing of the (200) planes as well as the tilting of (020) lattice planes. The color map of the d -spacing values corresponding to the image in Fig. 2c is displayed in Fig. 2e. The region with the missing data within the interphase boundary is due to the atomic blurring, likely from the fast phase propagation. Interestingly, we can identify mixed β -PdH_x and α -PdH_x phases within the expanded interface and the strain variations. Fig. 2f illustrates the local tilt angle of the (020) planes, obtained by fitting a line to the position of four atoms in the [100] direction. We find the lattice tilts around +5° relative to the vertical axis close to the upper phase propagation front and around -5° near the lower part of the interface. Remarkably, the observed lattice imperfection within the expanded interface (lattice tilting and mixture of α - and β -PdH_x phases) can be fully recovered to form a single crystal as the phase propagation proceeds. This further confirms that the formation of a unique expanded interface results from the lattice mismatch at the interface.

We conclude that the expanded interface with mixed α - and β -PdH_x phases accompanied by lattice tilting allows the crystal to compensate for the lattice mismatch strain during hydrogen absorption due to the fast phase propagation kinetics.

Dislocation motion at interfaces in slow kinetics

A representative high-resolution image of a Pd nanocube during hydrogen desorption is shown in Fig. 3a (from Supplementary Video 4). The co-existence of two phases is presented in the splitting {200} and {220} spots in the FFT pattern (Fig. 3a inset and Supplementary Fig. 18). The calculated d -spacing map of the (200) lattice planes clearly shows a sharp interface between the β - and α -PdH_x phases (Fig. 3b and Supplementary Fig. 18). The GPA (E_{yy}) strain map (Fig. 3c), superimposed on the interface region of the corresponding HRTEM image, reveals the sharp interface separating the β - and α -PdH_x. In the E_{xx} direction, the GPA data shows no significant strain variations at the sharp interface (Supplementary Fig. 19). A closer examination of the atomic arrangement at the interface reveals misfit dislocations (Fig. 3d,e). The inverse FFT images using the (020) spot (Fig. 3d) and the corresponding schematic representation (Fig. 3e) illustrate the positions of an edge dislocation in three consecutive frames. The analysis demonstrates the dynamic motion of misfit dislocation in both [100] and [010] directions at the prop-

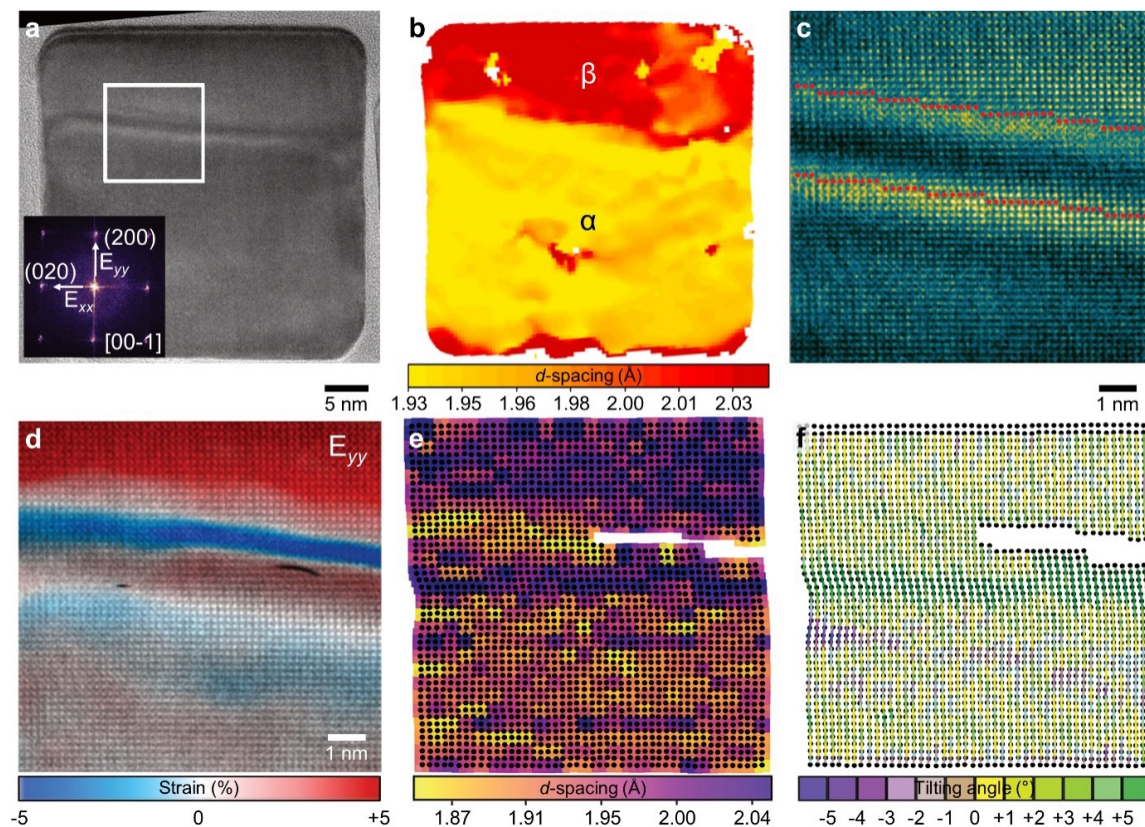


FIG. 2: Analysis of an expanded interface between α - and β -PdH_x during hydrogen absorption with fast phase propagation kinetics. **a**, An overview image of the Pd nanocube with the visible interface. The respective FFT pattern (inset) demonstrates the co-existing two crystal phases by the splitting reflections. **b**, The (200) d -spacing map of the Pd nanocube. **c**, An enlarged view of the selected region in **(a)** demonstrating the atomic structure at the interface. The last unaltered atomic columns at the interphase boundary are highlighted in red in both α - and β -PdH_x regions. **d**, GPA performed on the [100] (E_{yy}) direction based on the high-resolution image displayed in **(c)**. Compared with the smooth contrast in the regions of α -PdH_x (selected as GPA reference area) and β -PdH_x, drastic contrast changes within the expanded interface suggest significant d -spacing variations. **e,f**, The atomic arrangement analysis corresponding to the enlarged region in **(c)**. **(e)** The d -spacing variations of (200) planes. We can identify mixed β - and α -PdH_x phases within the expanded interface. **(f)** The tilting angle of (020) planes (obtained by linear fitting of four atomic columns).

agating sharp interface between β - and α -PdH_x during hydrogen desorption.

Simulations of kinetically tuned interface configurations

We employ an elastic Ising model to understand the observed differences in interface configurations under different phase propagation speeds. Our simulations are conducted in a rod-like geometry with one end of the rod held in α -PdH_x phase and the other in β -PdH_x phase.³⁹ In every trajectory, a rod of α -PdH_x is transformed into a rod of β -PdH_x with an interface that propagates in the positive z -direction. Kinetic Monte Carlo dynamics are used to evolve the system, with rates that include diffusion of β -phase within the rod, and the absorption and desorption of β -phase only at the interface. Within this framework of our constrained dynamic model, this rod

can be interpreted as the central part of a nanocube that possesses a greater spatial extent than the rod geometry (see **Supplementary Note 5** and **Extended Data Fig. 4**).

Within the model, the chemical potential difference, $\Delta\mu$, between the H₂ molecules in solution and the H atoms in the Pd lattice sets the driving force for interface propagation (see **Supplementary Note 5**). The configurations shown in **Fig. 4a,b** represent typical interfacial structures from trajectories under a chemical driving force of $\Delta\mu = 0.1 k_B T$ and $\Delta\mu = 1.0 k_B T$. When the chemical driving force is small compared to the thermal energy, diffusion occurs more quickly than absorption, and a narrower boundary between the two phases is maintained during propagation. However, when the chemical driving force is comparable to the thermal energy, absorption occurs too quickly for the surface to re-

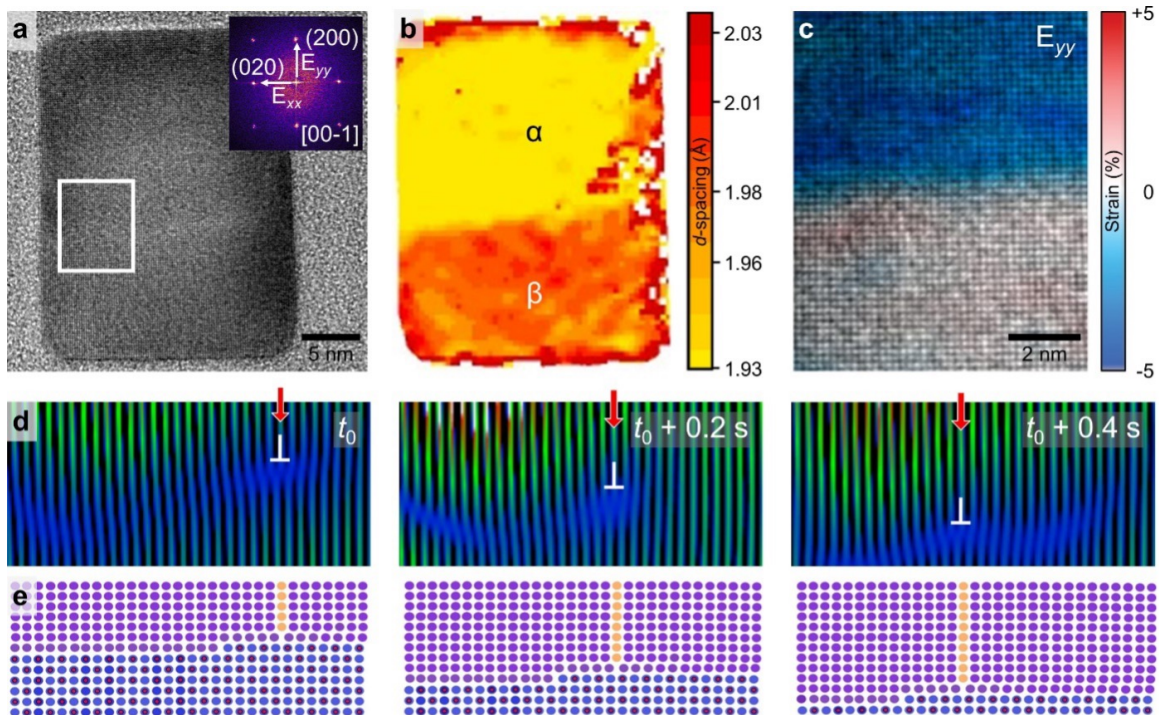


FIG. 3: Analysis of the atomic structure, strain, and misfit dislocation evolution at interfaces between α - and β -PdH_x during hydrogen desorption with slow phase propagation kinetics. **a**, High-resolution TEM image of a Pd nanocrystal during hydrogen desorption. The corresponding FFT pattern (inset) shows the presence of two phases. **b**, The calculated (200) d -spacing map of the Pd nanocrystal. **c**, GPA strain map overlaid on the magnified high-resolution image, which corresponds to the selected region in (**a**), demonstrates the sharp interface boundary between two smooth contrast regions of α -PdH_x and β -PdH_x in the [100] direction (E_{yy}). We set the bottom β -PdH_x area as reference for this GPA for the desorption case. **d**, Bragg filtering of the (020) reflection reveals dislocations at the interface in three consecutive frames during the hydrogen desorption reaction. The dislocation moves in both [100] and [010] directions. **e**, Schematic representation of the atomic structure evolution of the crystal lattice across the interface based on the experimental observation as displayed in (**d**). The propagation of the edge dislocation along with the interface is highlighted.

lax, and the boundary between the two phases becomes expanded. The instantaneous interface between the two phases can be defined more quantitatively as the isosurface where the concentration of β -PdH_x at coexistence (c_β) is 0.5 (see **Supplementary Note 5**). **Fig. 4c** shows a time series of the average position of this instantaneous interface in the rod, averaged over an ensemble of independent trajectories for both $\Delta\mu = 0.1 k_B T$ and $\Delta\mu = 1.0 k_B T$. Under each chemical driving force, we measure the average speed (see **Supplementary Note 5**) of the interface propagation, which increases monotonically with the driving force as expected (**Fig. 4d**). The increase in the average speed of propagation across the range of $\Delta\mu = 0.1$ - $1.0 k_B T$ is approximately one order of magnitude, akin to the observed difference in propagation speeds between absorption and desorption in our liquid phase TEM experiments. The width of the interface is computed from the mean squared deviations of the instantaneous interface along the direction of propagation, which is representative of the average size of the interphase region (see **Supplementary Note 5**). **Fig.**

4e shows that as the interface propagates more quickly it also becomes expanded, increasing by approximately 30% for the largest value of $\Delta\mu$ shown. In **Fig. 4b**, it is apparent that a typical configuration in the expanded regime ($\Delta\mu = 1.0 k_B T$) contains more (001) planes, which have both α - and β -phase unit cells. While the fact that our model contains only two components prevents the direct observation of mixed phases, it may be reasonable to assume that such incomplete layers would represent mixed phases within a more flexible model. The characterization of the degree of mixing between the α - and β -phases warrants further study with a finer-grained modeling approach. This model also includes only coherent interfaces. Thus, the experimentally observed expanded interface upon hydrogen absorption, relative to the slower desorption, can be attributed to a kinetic roughening^{40,41} and associated purely with faster propagation.

Our simulations of the dynamic phase transformations with a minimal model provide critical insights into the different interfacial structures observed in our liquid phase TEM experiments. The fast phase transfor-

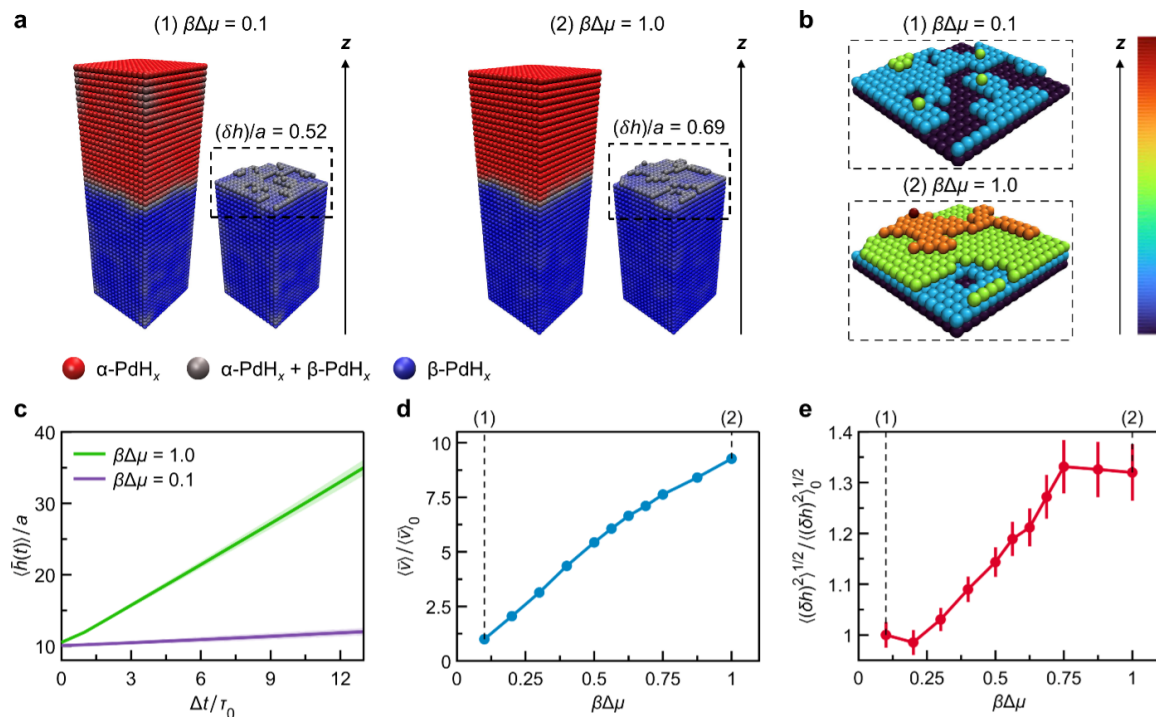


FIG. 4: Simulations of the dynamic phase transformations of α/β -PdH_x system under different phase propagation speeds using an elastic Ising model. **a**, Representative configurations from interfacial propagation trajectories under $\Delta\mu$ of 0.1 and 1.0 $k_B T$, in rods ($16 \times 16 \times 50$ unit cells): all unit cells and only those with the local value of $c_\beta > 0.5$. δh represents the instantaneous interfacial width in units of ‘ a ’, the model’s lattice constant. Propagation videos are **Supplementary Videos 5 and 6**. **b**, The interfacial regions (dotted boxes in (a)). Color indicates the location along the z -axis: zero set at the topmost (001) plane, with all unit cells having the local value of $c_\beta > 0.5$. **c**, Averaged time-series of the interface height for $\Delta\mu$ of 0.1 and 1.0 $k_B T$, with one standard deviation shaded. **d,e**, The average velocity of the interfacial surface in the z -direction (**d**) and its characteristic width (**e**) under increasing $\Delta\mu$. Error bars display two standard errors. (**c-e**) Angled brackets represent an ensemble average over at least 115 independent trajectories. The subscript zero denotes the average under the ensemble with $\Delta\mu = 0.1 k_B T$. When multiplying $\Delta\mu$, β is the inverse temperature.

mation pushes the system far-from-equilibrium, and the interface expansion and imperfection, analogous to interface roughening, is a generic route to accommodate mismatch strain under fast transformation kinetics. Under slow transformations, smooth interfaces are observed, suggesting the system is near-equilibrium.

Conclusion

By utilizing liquid phase TEM, we have achieved unprecedented atomic resolution imaging of hydrogen-induced phase transformations in Pd nanocrystals, which allows us to reveal distinct atomic pathways for mismatch strain relaxation at interfaces under phase transformation kinetics differing by about an order of magnitude. We have discovered a generic route to compensate for mismatch strain by expansion and imperfection (*e.g.*, mixing of phases, lattice tilting, or other defects) of the interfaces under fast phase transformations in a far-from-equilibrium regime. This extends our conventional understanding of dislocation formation as the standard mechanism to release mismatch strain at interfaces.

The expanded interface is configured as the lattice tilting up to $\pm 5^\circ$ near the phase propagation front, two-phase mixture, and other defects. This is distinctly different from the near-equilibrium phase transformation, where the interface is sharp, accompanied by the misfit dislocation movements at the interfaces. Our findings provide valuable insights into engineering materials with desired structures and functionalities. For example, through far-from-equilibrium material processing techniques, we can synthesize materials rich in lattice imperfections, thus providing abundant catalytic active sites. Conversely, near-equilibrium processing may create defect-free materials more effective for hydrogen storage and purification, or electrochemical ion insertion devices. Moreover, our capability to directly observe atomic-level dynamics in systems far-from-equilibrium opens future opportunities for identifying metastable structures and leveraging intermediate phases to tune kinetic pathways across a broad range of significant physicochemical processes of materials.

Acknowledgments

This work was supported by the U.S. Department of Energy, Office of Science, Office of Basic Energy Sciences (BES), Materials Sciences and Engineering Division under Contract No. DE-AC02-05-CH11231 within the in-situ TEM program (KC22ZH). Work at the Molecular Foundry of Lawrence Berkeley National Laboratory (LBNL) was supported by the U.S. Department of Energy under Contract No. DE-AC02-05CH11231. S.B.B. acknowledges financial support from the Alexander-von-Humboldt Association. D.L. acknowledges the Kwanjeong Study Abroad Scholarship from the KEF (Kwanjeong Educational Foundation) (KEF-2019). S.B.B. thanks Prof. A. Paul Alivisatos for discussions. We thank Dr. Karen C. Bustillo for her help with the electron microscope setup.

Author Contributions

S.B.B. did the liquid phase TEM experiments. S.B.B., D.L., and C.O. performed the experimental data analysis. S.O.L. carried out the theoretical modeling and simulations and analyzed results under the supervision of D.T.L. This paper was written by S.B.B., D.L., S.O.L., D.T.L., and H.Z. with input from all co-authors. H.Z. conceived and supervised the project.

Competing Interests

Authors declare that they have no competing interests.

Correspondence

Correspondance and requests for materials should be addressed to H. Zheng (hmzheng@lbl.gov) or D. T. Limmer (dlimmer@berkeley.edu).

Methods

Synthesis of palladium nanocubes

Palladium nanocubes with sizes between 40 and 50 nm are synthesized using a reported two-step synthesis strategy.²⁵ In the first step, the seed solution is synthesized: 91.1 mg cetrimonium bromide (CTAB from Sigma-Aldrich) is dissolved in 20 mL H₂O by stirring (400 rpm) at 95 °C for 5 minutes. A 10 mM H₂PdCl₄ solution is prepared by dissolving 10.7 mg anhydrous PdCl₂ (Sigma-Aldrich) in 5 mL of 20 mM HCl (Sigma-Aldrich). 1 mL of this 10 mM H₂PdCl₄ solution is added to the CTAB solution, which subsequently turns red. The mixture is stirred for 5 minutes before adding 160 μ L of a 100 mM L-ascorbic acid solution (created by dissolving 17.6 mg L-ascorbic acid from Sigma-Aldrich in 1 mL H₂O). The final mixture is stirred for 5 min at 95 °C before being placed in an ice bath to stop the reaction.

In the second step, the nanocube size is increased to 40 and 50 nm from the seeds; for this, a 0.1 M CTAB solution is prepared by dissolving 364.5 mg CTAB in 10 mL H₂O. This CTAB solution is heated to 60 °C before adding 125 μ L of the 10 mM H₂PdCl₄ solution, 100

μ L of the seed solution, and 50 μ L of the 100 mM L-ascorbic acid solution. The mixture is slightly shaken and allowed to sit for 2 hours at 60 °C. The final product is collected by centrifugation at 6000 rpm for 5 minutes and washed twice with 5 mL H₂O using a centrifugation rotation speed of 10000 rpm. Overview images, including bright-field transmission electron microscopy (TEM) and energy-dispersive X-ray spectroscopy (EDS) map images, of synthesized nanocubes are displayed in **Supplementary Fig. 1**. Detailed crystallographic properties of a synthesized Pd nanocube are demonstrated in **Supplementary Fig. 2**.

High-resolution liquid cell fabrication

The liquid cells used in this study are based on Formvar-coated TEM grids. The Formvar films are fabricated according to the following protocol. First, a microscope glass slide is dipped into a 0.25% Formvar solution in ethylene dichloride (Electron Microscopy Sciences), resulting in a thin film coating the glass slide (**Supplementary Fig. 3a**). The film is dried in the air for 5 minutes. Subsequently, the surface tension of water is exploited to separate the Formvar film from the glass slide (**Supplementary Fig. 3b**). The Formvar film floats on the water's surface, and Cu TEM grids (Electron Microscopy Sciences) are dropped onto the film's surface (**Supplementary Fig. 3c**). Finally, the Formvar-coated grids are collected with a second glass slide and dried at ambient conditions (**Supplementary Fig. 3d**). Electron energy-loss spectroscopy demonstrates a reproducible thickness of 17 ± 3 nm for the synthesized Formvar films.

Then, 1 μ L of the aqueous solution containing palladium nanocubes is drop-casted onto the Formvar-coated TEM grids. The TEM grids are subsequently plasma-cleaned in an Argon-Oxygen atmosphere (Fischione Model 1020 plasma cleaner) for 8 seconds. The plasma cleaning makes the films hydrophilic, reduces the film thickness by about 40%, and removes the residual organic ligands from the nanoparticle surface. Then, 0.5 μ L of 0.1 M KOH (Sigma-Aldrich) is dropped onto one TEM grid. A filter paper is used to remove the excess liquid so that only a thin liquid layer covers the grid. Subsequently, a second TEM grid is placed, and the liquid cell is sealed by the van-der-Waals attraction between the films. Liquids are trapped within small pockets formed between the membranes of the two grids.

Transmission electron microscopy

The FEI ThemIS 60-300 (Thermo Fisher Scientific) transmission electron microscope with an X-FEG gun operated at 200 and 300 kV was used for *in situ* TEM experiments. The microscope is equipped with an image aberration corrector (spatial resolution limit of 70 pm), Bruker SuperX energy-dispersive X-ray spectroscopy (EDS) detector (solid angle of 0.7 steradians), and a Ceta2 CMOS camera. The FEI F20 Tecnai microscope was used to record electron energy loss spec-

troscopy data.

Determination of the H₂ concentration as a function of the electron dose rate

A quasi-stationary model⁴² is used to describe the growth/dissolution of gas bubbles in supersaturated/undersaturated solutions. The model describes the changes in the bubble radius $r(t)$ due to the mass transport of the gaseous species into/out of the bubble, neglecting the surface tension. Bubbles grow if the concentration of the gaseous species dissolved in a liquid (c_i) exceeds its saturation concentration in the liquid (c_s).⁴³ By depleting the supersaturated c_i , the bubbles grow until the gas concentration inside the liquid reaches its saturation concentration c_s . We track the changes in the bubble radius with time as a function of the electron dose rate to establish an understanding of the H₂ and O₂ concentrations during the *in situ* experiments. An exemplary TEM image is shown in **Supplementary Fig. 4a** highlighting the identified gas bubbles. Ellipses are fitted to the bubbles in the image to account for the non-spherical shape of some bubbles. The spherical radius r_s of the bubble is related to the two radii r_1 and r_2 characterizing an ellipse (see **Supplementary Fig. 4b**): $r_s = \sqrt{r_1 r_2}$. Dynamic changes of individual bubbles are reflected by a large size distribution within one TEM image. **Supplementary Fig. 4c** illustrates the radii detected at distinct times during an *in situ* liquid phase experiment. Considering that the supersaturation of the solution is reflected by the size of the largest bubbles, we track the average of the 25% largest bubbles as a function of the dose rate or illumination time (highlighted in red in **Supplementary Fig. 4c**). The analysis of the radius change as a function of the reaction time at a constant electron dose rate demonstrates that the bubble radius approaches a steady-state size (**Supplementary Fig. 4d**), which depends on the electron dose rate used during the experiment (**Supplementary Fig. 5**). The time for establishing the steady-state concentration varies randomly and does not follow the expected trend; for example, the higher the dose rate, the shorter the time. This is likely due to the different sizes of the investigated liquid pockets in the liquid cell. Since only a small subsection of the liquid cell is illuminated by the beam during liquid phase TEM experiments, the mass transport outside the illuminated area impacts the steady-state concentrations.^{28,31}

High-resolution TEM (HRTEM) image analysis – a rolling window algorithm

As shown in **Supplementary Fig. 6**, palladium’s lattice expansion due to hydrogen absorption is represented in the changes in radial distances of reflections in the diffractogram. In other words, we can differentiate α - and β -PdH_{*x*} phases during hydrogen-induced phase transformations based on the differences in d -spacing values. To trace local variations of the d -spacing within the palladium nanocubes during the phase transformations, we developed a rolling window algorithm inspired by previ-

ous work⁴⁴ (**Supplementary Fig. 7**). This algorithm utilizes dynamically moving windows over HRTEM images, which generate fast Fourier transformation (FFT) patterns corresponding to local regions of Pd nanocubes, determining the d -spacing variations (*i.e.*, the spatial distributions of α - and β -PdH_{*x*} phases) based on the FFT patterns. Fitting 2D Gaussian functions to the FFT pattern allows the determination of peak positions with sub-pixel accuracy. The determined d -spacing values are used to generate maps visualizing the variations in the lattice arrangements within the nanoparticles. The fitted patterns with variations more significant than the angle variation of $\pm 5^\circ$ and the d -spacing variation of $\pm 0.1 \text{ \AA}$ are discarded. The window size of the FFT pattern determines the spatial resolution, and the values of 10×10 pixels are averaged to generate the maps. Additionally, a mask segmenting the nanoparticle from the amorphous background is used to remove artifacts created by the amorphous structure.

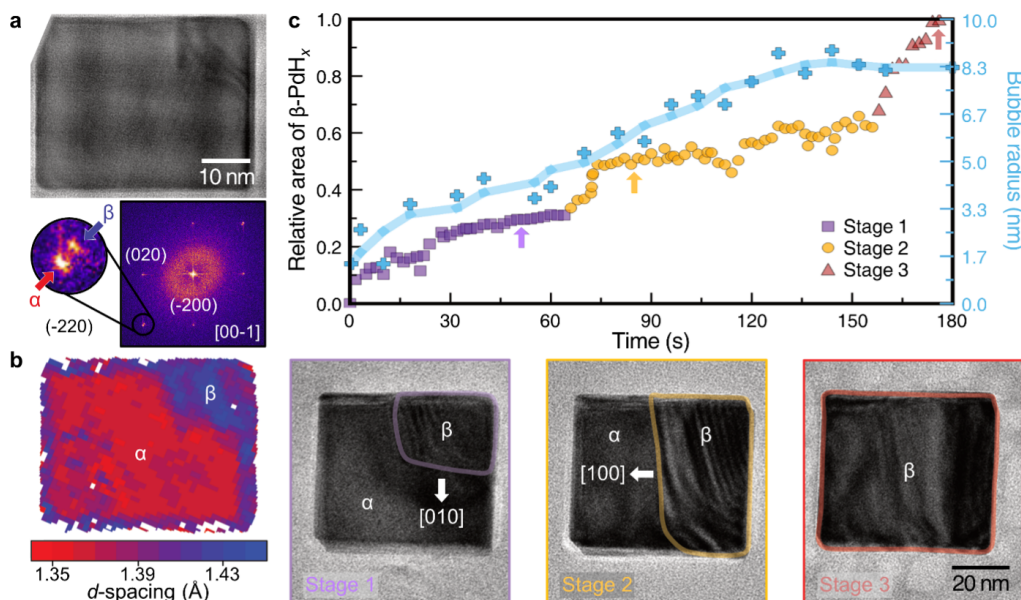
Geometric phase analysis (GPA)

GPA was used to investigate strain at interphase boundaries within palladium nanocubes during hydrogen absorption and desorption reactions. The GPA method measures the displacement of lattice fringes shown in HRTEM images of palladium nanocubes during the hydrogen-induced phase transformations. We select the parts of nanocrystals below their interphase boundaries as references. In other words, we choose the α -PdH_{*x*} and β -PdH_{*x*} as references for the absorption and desorption cases, respectively. Then, compute the differences in d -spacing values throughout an HRTEM image to generate a corresponding strain map. Finally, the strain distributions are revealed in **Figs. 2d and 3c** and **Supplementary Figs. 17 and 19**.

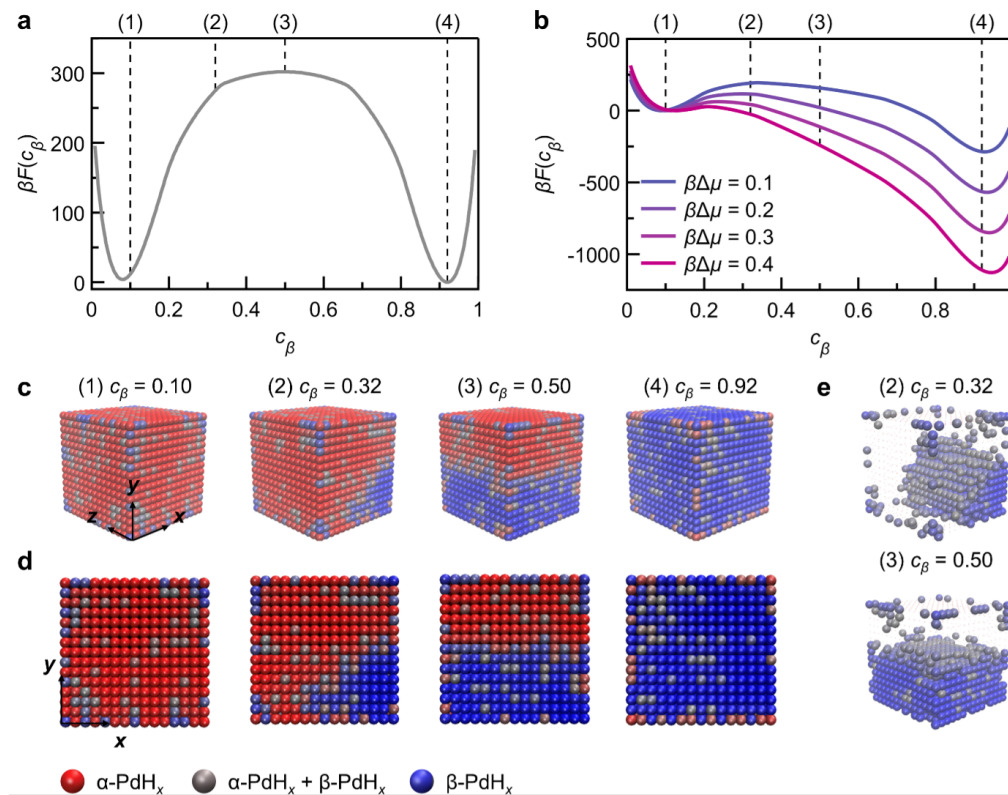
Data and Code Availability

All data and codes that support the findings of this study are available from the corresponding authors upon reasonable request.

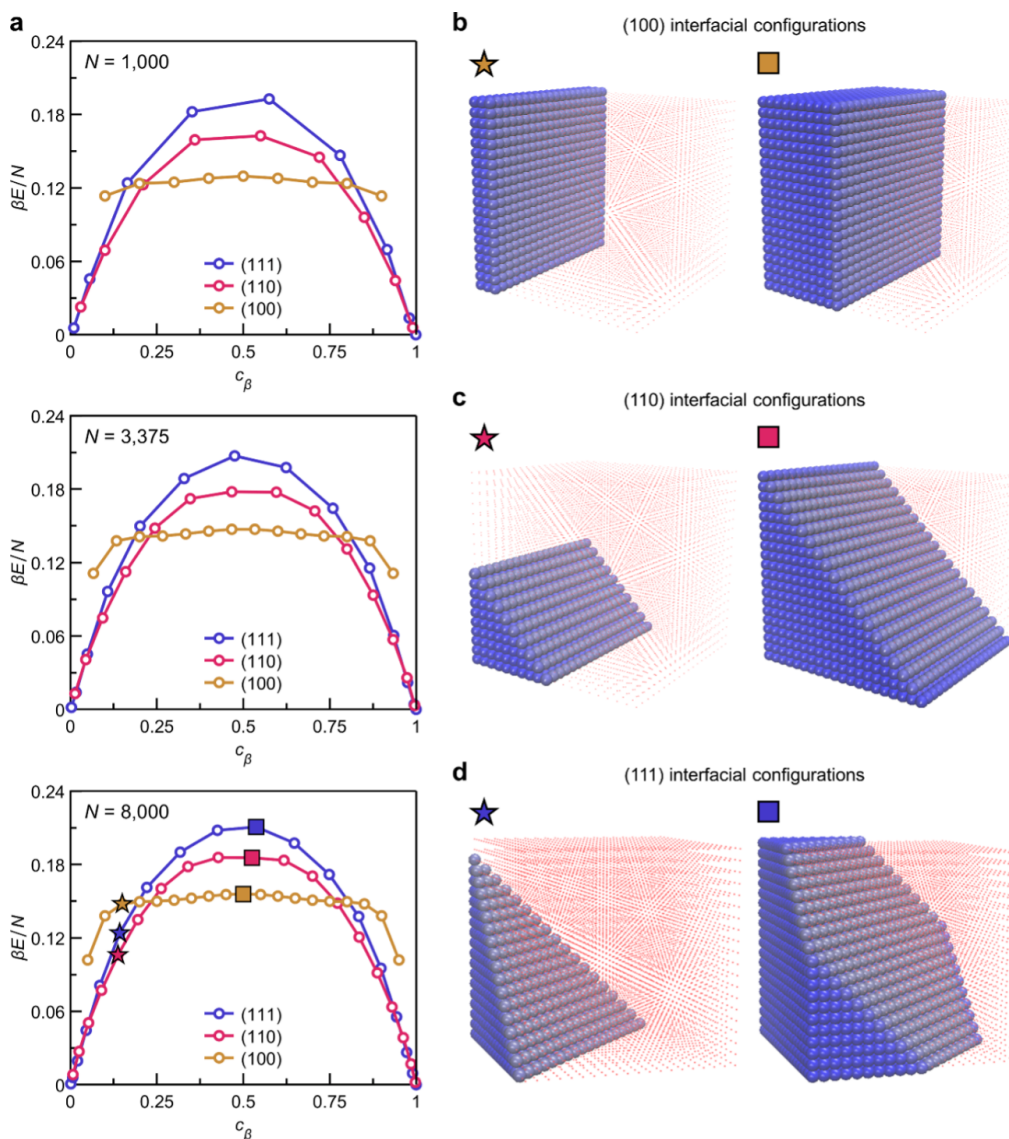
Extended Data



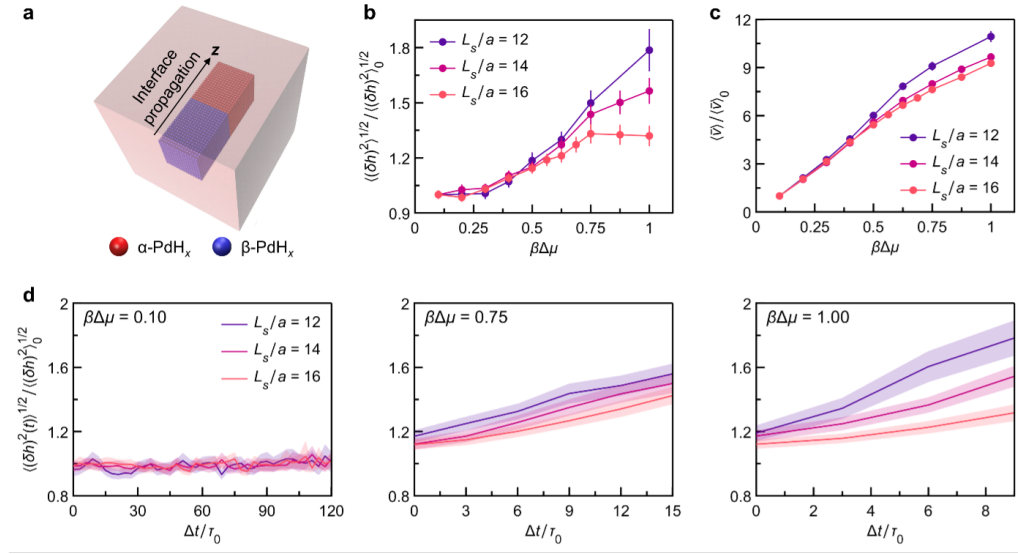
Extended Data Fig. 1. The nucleation and propagation of the β -PdH_x phase in Pd nanocubes during hydrogen absorption. **a**, HRTEM image of a Pd nanocube at the initial state of the hydrogen absorption reaction. The respective FFT pattern shows the presence of two crystal phases (α and β phases) as indicated by a splitting of the (-220) diffraction spots. **b**, The analysis of the spatial variation of the d -spacing of (-220) reveals the local lattice expansion at the upper right corner of the nanocube. The local lattice expansion induces strain and a local thickness variation, resulting in the dark fringes in the respective TEM image. **c**, Phase transformation dynamics determined based on the relative area of the nanocube covered by the dark fringes (*i.e.*, the relative area of the β -PdH_x) and the bubble radius, which is proportional to hydrogen concentration (**Supplementary Video 1**). The reaction happens in three stages, highlighted in purple, yellow, and red. The displayed TEM images are characteristic of the nanocube during the three different stages (designated by colored arrows). The experiment time is given relative to the initial data acquisition.



Extended Data Fig. 2. Free energy curves for hydrogen absorption and configurations along a reversible absorption pathway in the model. **a**, The Helmholtz free energy as a function of c_β computed from standard umbrella sampling techniques and the weighted histogram analysis method. All simulations are run at temperature (T) = 300 K (complete simulation details in **Supplementary Note 3**). **b**, The same free energy curves as in (**a**), but with linear shifts due to chemical potential differences, $\Delta\mu$, between H_2 molecules in the surrounding solution and H atoms in the palladium lattice. One sees the corner nucleated configuration, (2), is a representative critical nucleus when chemical driving for absorption is on the order of one-tenth the thermal energy. Note that, when multiplying an energy, β represents the inverse temperature. **c,d**, Two perspectives on representative configurations taken from umbrella sampling trajectories, with c_β increasing in each configuration from left to right. **e**, The same configurations, (2) and (3) from (**c and d**), where only unit cells with a local value of c_β greater than 0.5 are shown to visualize the full interphase boundaries.



Extended Data Fig. 3. An energetic analysis of idealized configurations along hypothetical absorption pathways. **a**, The elastic energies (**Supplementary Equation 2** in **Supplementary Notes 2.2**) of idealized (100), (110), and (111) interfacial configurations as a function of c_β , at three different sizes of nanocube. N is the total number of sites, and β represents the inverse temperature when multiplying an energy. **b,c,d**, Selected configurations with labels corresponding to the markers in the third panel of (**a**).



Extended Data Fig. 4. Analysis of the size dependence of the interfacial propagation in rod geometries. **a**, A schematic of how a rod can be viewed as the core of a larger nanocube. **b,c,d**, L_s denotes the width of the rod in the x - y dimensions in units of ‘ a ’, the model’s lattice constant. The length in the z -direction is 50 unit cells for all data. **b** Average interfacial widths under increasing chemical driving force. **c** Average velocities under increasing chemical driving force. (**b and c**) Averages recorded over the range $\bar{h}/a = 25$ to $\bar{h}/a = 31$. **d** Time series of the width under three chemical driving forces. Δt is recorded from the time the interface reaches an average height of $\bar{h}/a = 10$. The zero subscript denotes the average under the ensemble with $\Delta\mu = 0.1k_B T$.

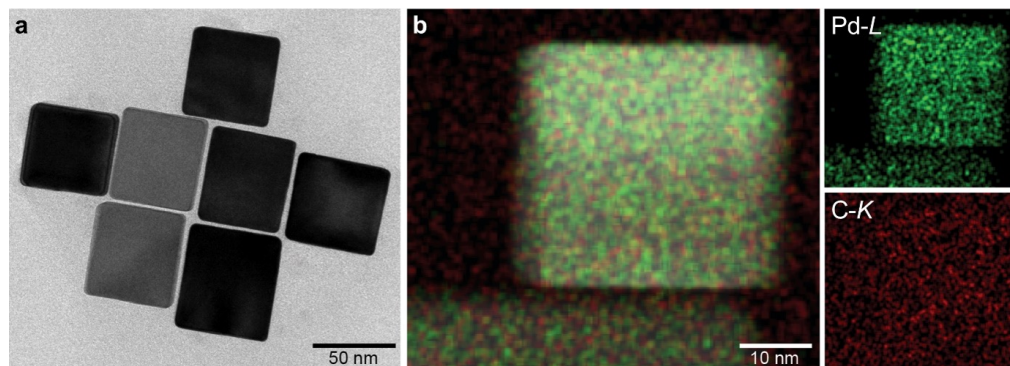
Supplementary Notes

1. Hydrogen absorption pathway in palladium nanocubes

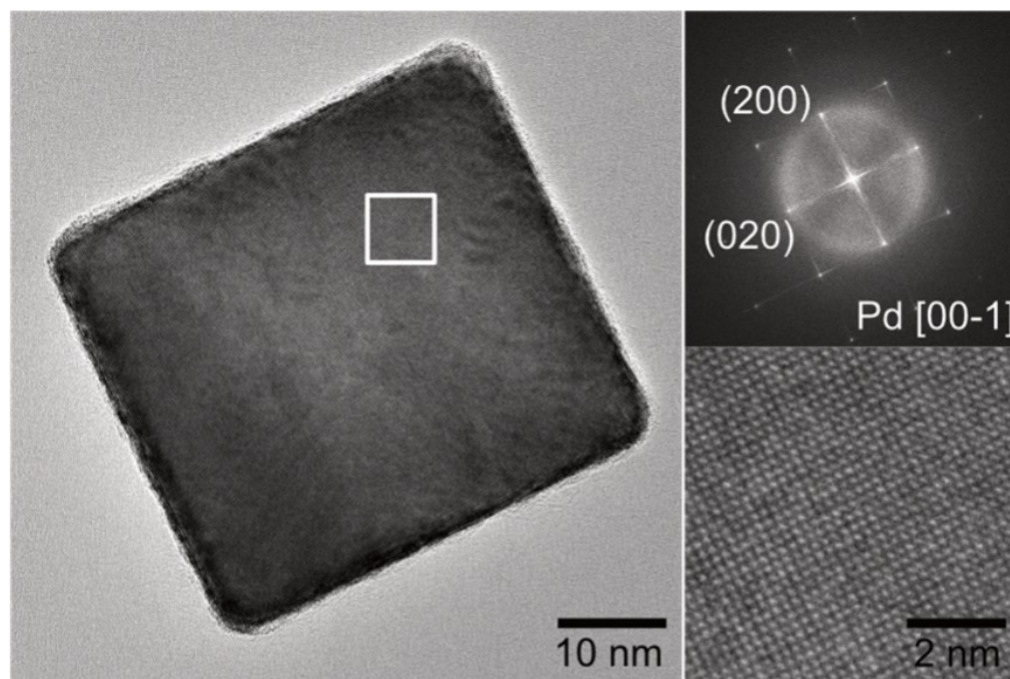
Extended Data Fig. 1a shows a high-resolution TEM image of a Pd nanocube recorded during the initial period of the hydrogen absorption reaction. The FFT pattern shows the co-existence of α - and β -PdH_x phases indicated by the splitting of the (-220) diffraction spots (as described in **Supplementary Fig. 6c**). High-resolution image analysis with the rolling window algorithm tracking the spatial distribution of the two crystal phases in the Pd nanocube (see **Methods** and **Supplementary Fig. 7**) demonstrates that the lattice expansion (β -PdH_x phase) is localized at the upper right corner of the nanocube (**Extended Data Fig. 1b**), coinciding with the dark fringes in the image. Similar fringes were previously observed in the dark-field scanning TEM (STEM) experiments on hydrogen absorption in a gas atmosphere.²² These fringes result from either the strain induced by the lattice mismatch between α and β -PdH_x or the thickness increase induced by the local swelling of the crystal lattice.

We utilize the fringes to identify the hydrogen uptake into palladium nanocubes at lower magnification (**Supplementary Video 1**). **Extended Data Fig. 1c** shows the kinetics of the phase transformation induced by the hydrogen absorption in a Pd nanocube, quantifying the area of the dark fringes. During this *in situ* experiment, the electron flux was stepwise increased to manipulate the H₂ concentration. The hydrogen concentration can be correlated with the average bubble radius (see **Methods** and **Supplementary Figs. 4 and 5**). Coupled with the time-series data of the average bubble radius, the analysis of the proportion of β -PdH_x (calculated by the projected area of dark fringes) with time demonstrates three stages of hydrogen absorption in the palladium nanocrystal (**Extended Data Fig. 1c**).

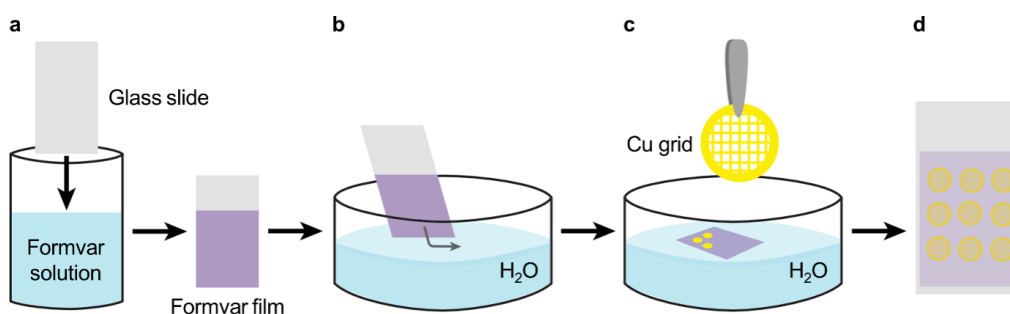
From the nucleation of β -PdH_x at the corner of the palladium nanocube to 25% of the nanocube being transformed into β -PdH_x (Stage 1), the β -PdH_x is localized at the corner. Increasing the electron dose rate promotes the hydrogen absorption reactions, since more hydrogen can be produced, as indicated by the increased bubble radius. After a short reaction stagnation, the phase propagation proceeds rapidly along the [010] direction until about 50% of the nanocube is transformed to β -PdH_x (Stage 2). The phase transformation slows again until the rapid phase propagation along the [100] direction completes the phase transformation within a few seconds (Stage 3). Although our analysis is limited to the 2D projections of three-dimensional nanocubes, it is evident that the phase transformation from Stage 1 to Stage 2 and Stage 3 requires a change of the phase propagation direction. Our experimental data demonstrate the corner nucleation and [100] propagation of β -PdH_x during hydrogen absorption in palladium nanocubes, which aligns with the results reported in preceding studies.^{22,25}



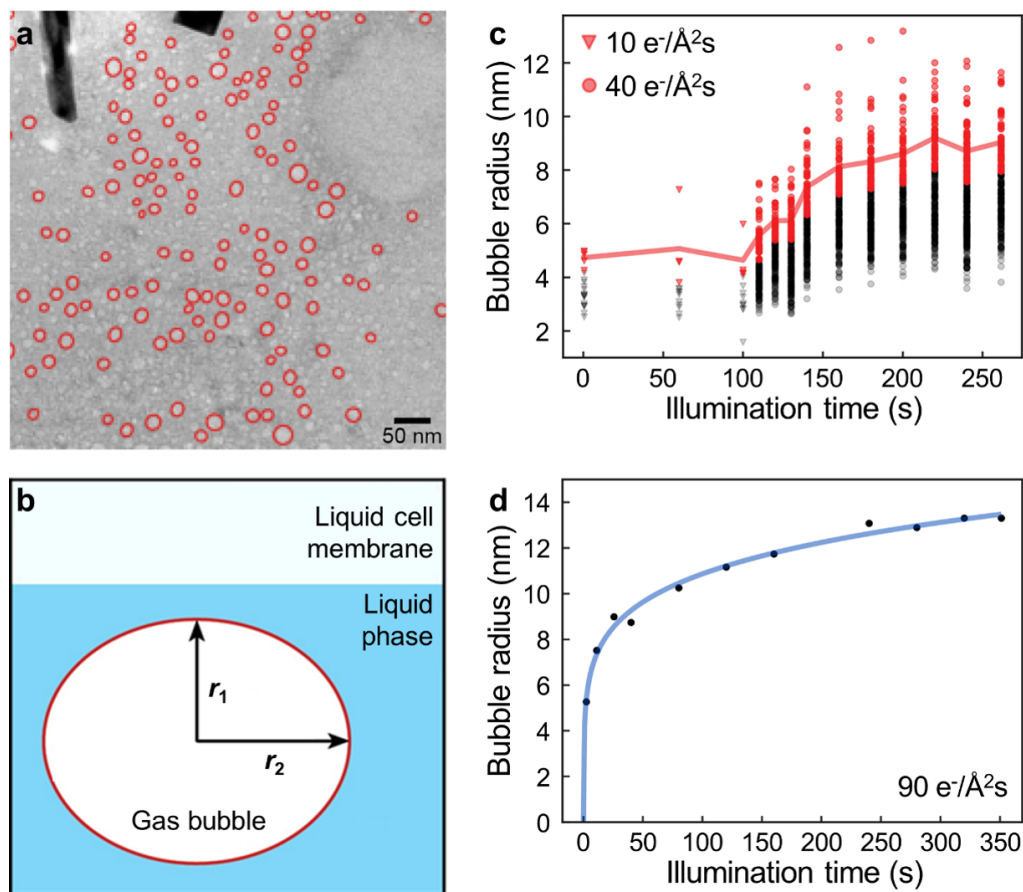
Supplementary Fig. 1. S/TEM characterizations of as-synthesized palladium nanocubes. **a**, Bright-field TEM image of several palladium nanocubes on an amorphous carbon film synthesized following the described procedure. **b**, STEM image of palladium nanocubes overlaid with EDS maps (left) and corresponding Pd-L and C-K edges EDS maps (right), which confirm the purity of the palladium nanocubes and the absence of a carbon ligand shell.



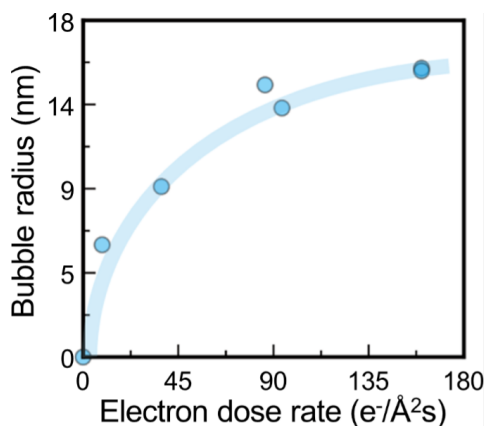
Supplementary Fig. 2. Crystallographic characteristics of a synthesized palladium nanocube. HRTEM image (left) of a palladium nanocube with a 40 to 50 nm size range, exposing the $\{100\}$ surface facets. The corresponding FFT pattern and magnified HRTEM image (right) exhibit the single-crystalline nature of the nanocube.



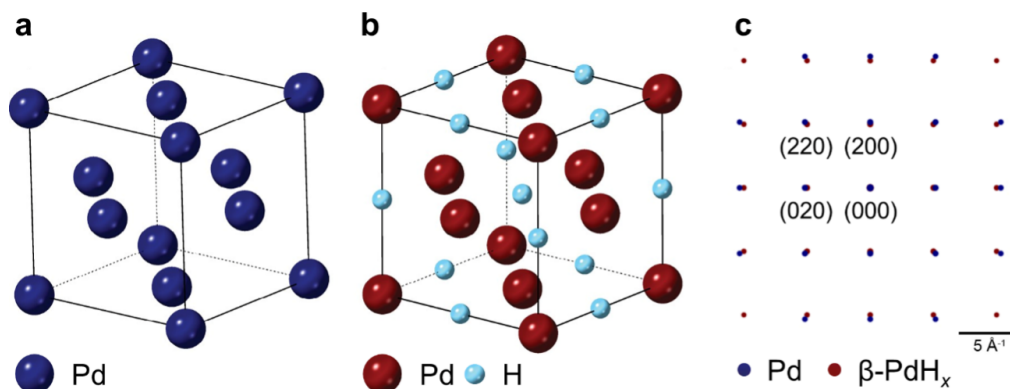
Supplementary Fig. 3. Schematic representation of the fabrication of Formvar-coated TEM grids. **a**, A glass slide is dipped into a 0.25% Formvar solution, resulting in a thin Formvar film coating the glass slide. **b**, The surface tension of water is used to separate the Formvar film from the glass slide. **c**, The Formvar film floats on water, and the TEM grids are placed on top of it. **d**, A second glass slide is used to catch the coated TEM grids.



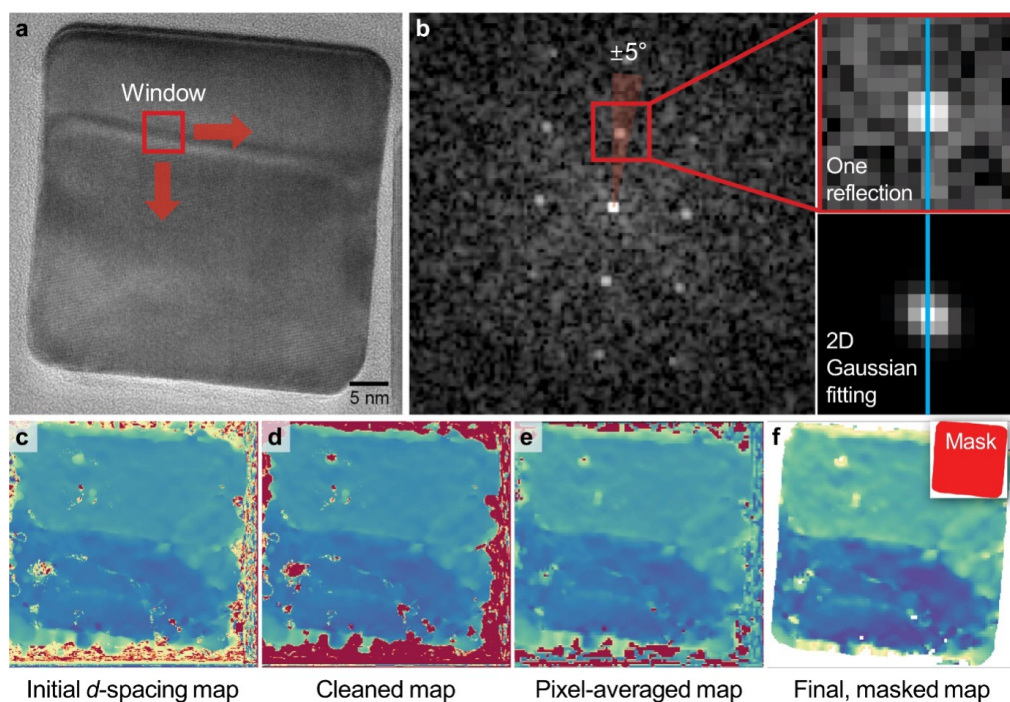
Supplementary Fig. 4. The H_2 concentration inside the liquid cell is indirectly estimated based on the size of the bubbles formed inside the liquid. **a**, A representative TEM image used for the bubble size analysis. The identified bubbles are highlighted in red. A dose rate of $40 \text{ e}^- \text{ \AA}^{-2} \text{ s}^{-1}$ was used to record this TEM image. **b**, Schematic presentation of the liquid cell conditions. Ellipses are fitted to the identified bubbles to account for their non-perfect spherical shapes. **c**, Scatter plot illustrating the identified bubble radii at different stages of the liquid phase experiment. The 25% largest radii are highlighted in red. These radii are used to determine the average radius as a function of reaction time, which is represented by the red line in the graph. The dose rate was increased from 10 to $40 \text{ e}^- \text{ \AA}^{-2} \text{ s}^{-1}$ during the experiment. **d**, Change of the average bubble radius as a function of time during an experiment performed at a constant dose rate of $90 \text{ e}^- \text{ \AA}^{-2} \text{ s}^{-1}$. The radii change rapidly during the first 60 s of the illumination and subsequently approach a steady state.



Supplementary Fig. 5. Electron-dose-rate-dependent gas bubble sizes. The steady-state average radius of the gas bubbles depends on the electron dose rate.



Supplementary Fig. 6. Crystal structures of palladium and β -PdH_x and their corresponding electron diffractograms. **a,b**, Schematic representations of the crystal lattices of Pd (**a**) and β -PdH_x (**b**). **c**, The incorporation of hydrogen into the lattice causes the lattice expansion of palladium by about 3.5% in the lattice parameter.^{15,16} This expansion is visible in the simulated diffraction patterns, in terms of radial distances of reflections for Pd (blue) and β -PdH_x (red). Please note that given that the difference in such radial distances between Pd and α -PdH_x is immeasurably small, under our *in situ* liquid phase experimental conditions, we can regard Pd as α -PdH_x.



Supplementary Fig. 7. Overview of the steps involved in the determination of the local variations of the d -spacing within individual Pd nanoparticles. **a**, A rolling window algorithm uses dynamically moving windows (a red box showing an example window) over the nanocube to determine the position of reflections in generated FFT patterns from those windows. **b**, An exemplary FFT pattern generated based on a moving window, which shows an allowed angle variation and fitting 2D Gaussian functions to a reflection. **c**, The initially obtained spatial d -spacing variation within the individual nanoparticle. **d**, Falsely identified values are removed by allowing an angle variance of $\pm 5^\circ$ and a d -spacing variance of $\pm 0.1 \text{ \AA}$. **e**, Since the resolution is limited by the window size used during the analysis, the d -spacing values are averaged for several pixel values. **f**, Artifacts created by the amorphous background are removed using a mask tool separating the nanoparticle from the background.

2. Details of elastic Ising model for the PdH_x system

2.1. Parameterization of the Hamiltonian

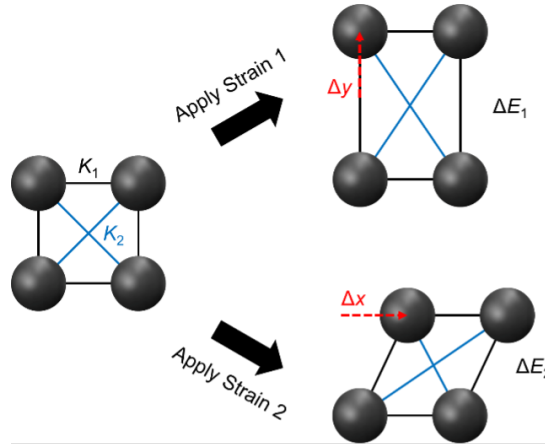
The elastic Ising model was used to model the interconversion of the α -PdH_x and β -PdH_x phases. This simple model includes harmonic interactions between both nearest and next-nearest neighbors on a simple cubic lattice. The Hamiltonian is given by a sum over lattice positions, \mathbf{R} ,

$$H = \sum_{\mathbf{R}} \left[\frac{K_1}{4} \sum_{\hat{\mathbf{a}}(\mathbf{R})} [|a\hat{\mathbf{a}} + \mathbf{u}_{\mathbf{R}} - \mathbf{u}_{\mathbf{R}+a\hat{\mathbf{a}}} | - l(\sigma_{\mathbf{R}}, \sigma_{\mathbf{R}+a\hat{\mathbf{a}}})]^2 + \frac{K_2}{4} \sum_{\hat{\gamma}(\mathbf{R})} [| \sqrt{2}a\hat{\gamma} + \mathbf{u}_{\mathbf{R}} - \mathbf{u}_{\mathbf{R}+\sqrt{2}a\hat{\gamma}} | - l(\sigma_{\mathbf{R}}, \sigma_{\mathbf{R}+\sqrt{2}a\hat{\gamma}})]^2 \right] \quad (1)$$

The set of unit vectors $\{\hat{\mathbf{a}}(\mathbf{R})\}$ points from site \mathbf{R} to the nearest neighbors of \mathbf{R} on the simple cubic lattice. For a bulk lattice site, there are six vectors, while generally there are fewer for sites at the edge of the cube. The set of unit vectors $\{\hat{\gamma}(\mathbf{R})\}$ point to the next-nearest neighbors of site \mathbf{R} , totaling 12 for a bulk lattice site. The variables $\{\mathbf{u}_{\mathbf{R}}\}$ represent displacements of site \mathbf{R} from its equilibrium position. When site \mathbf{R} is viewed as a unit cell of the Pd nanocube, $\{\mathbf{u}_{\mathbf{R}}\}$ represents a compression or expansion of the cell. The variables $\{\sigma_{\mathbf{R}}\}$ are the spins variables and take values ± 1 , with $+1$ corresponding to a unit cell that is locally β -PdH_x and -1 corresponding to a unit cell that is locally α -PdH_x. $l(\sigma_{\mathbf{R}}, \sigma_{\mathbf{R}'})$ is the preferred distance between two sites, which, due to the expansion of the lattice in the β phase, depends on the values of the spin variables. We take $l(\sigma_{\mathbf{R}}, \sigma_{\mathbf{R}'}) = a_0 + \Delta/2 + \Delta/4(\sigma_{\mathbf{R}} + \sigma_{\mathbf{R}'})$, where a_0 is the equilibrium lattice constant of bulk Pd and Δ is approximately 3.5% of this value (**Supplementary Table 1**).

The values for the spring constants, K_1 and K_2 , were chosen such that the model could reproduce the response of bulk Pd to a longitudinal stretch and a pure shear. To do so, we considered a $2 \times 2 \times 2$ cube of sites in the model. The corners of our cube are connected by springs with stiffnesses given by K_1 and K_2 (**Supplementary Fig. 8**). We assume our system is tiled by such cubes, and we account for the fact that the springs of one cube are shared by the neighboring cubes. This means that the springs with stiffness K_1 have a weight of one-fourth, and that the springs of stiffness K_2 have a weight of one-half.

If all sites are the same spin, then a configuration with no strain will make all side lengths of the cube equal to l , the lattice constant for that phase. We apply a stretch and a shear strain to the cube and calculate the energetic cost according to **Supplementary Equation 1**. This gives us $\Delta E_1 = (K_1 + 2K_2)\Delta y^2/2$ and $\Delta E_2 = K_2\Delta x^2/2$, while elastic theory gives $\Delta E_1/l^3 = c_{11}(\Delta y/l)^2/2$ and $\Delta E_2/l^3 = c_{44}(\Delta x/l)^2/2$. Therefore, a consistent choice for the spring constants are, $K_1 = l(c_{11} - 2c_{44})$, and $K_2 = lc_{44}$. Hsu and Leisre⁴⁵ have calculated the low-temperature limits of the elastic moduli of PdH_x in both the α and β phases. Since we have created our mapping considering only the energetic cost rather than the free energy, we take the 0 K extrapolations for c_{11} and c_{44} . Since we wish to model the regime of coexistence, we take averages of the α and β phase values for both the value of l and the elastic moduli. This procedure provides the parameters listed in **Supplementary Table 1**.



Supplementary Fig. 8. Depiction of the two applied strains used to parameterize the model Hamiltonian as described in **Supplementary Note 2.1**.

Parameter	Value
Δ	0.1387 Å
a_0	0.3890 Å
K_1	2.2303 eV/Å ²
K_2	1.7307 eV/Å ²

Supplementary Table 1: Parameters used for the Hamiltonian (**Supplementary Equation 1**) based on experimental data from the reference.⁴⁵

2.2. Small mismatch approximation and effective interaction potential

By linearizing the absolute value terms in **Supplementary Equation 1**, one obtains a Hamiltonian in the limit of a small lattice mismatch between the two phases⁴⁶ that is quadratic in the displacement variables. We can make the further assumption that vibrations of the lattice relax quickly compared to typical timescales of diffusion of hydrogen between lattice sites. This allows us to analytically integrate out the displacement variables, yielding an effective interaction potential among only the spin variables,³⁵ of the form,

$$H_{\text{eff}} = \frac{1}{2} \sum_{\mathbf{R}, \mathbf{R}'} \sigma_{\mathbf{R}} \mathbf{V}_{\mathbf{R}, \mathbf{R}'} \sigma_{\mathbf{R}'} \quad (2)$$

where spins are coupled by an effective long-range potential. The spin-spin potential, $\mathbf{V}_{\mathbf{R}, \mathbf{R}'}$, is given by a sum of two terms,

$$\mathbf{V}_{\mathbf{R}, \mathbf{R}'} = \left(\mathbf{S} - \frac{1}{4} \mathbf{C}^T \cdot \mathbf{D}^{-1} \cdot \mathbf{C} \right)_{\mathbf{R}, \mathbf{R}'}$$

a term,

$$\mathbf{S}_{\mathbf{R}, \mathbf{R}'} = \frac{K_1 \Delta^2}{16} \sum_{\hat{\alpha}(\mathbf{R})} (\delta_{\mathbf{R}, \mathbf{R}'} + \delta_{\mathbf{R}+a\hat{\alpha}, \mathbf{R}'}) + \frac{K_2 \Delta^2}{8} \sum_{\hat{\gamma}(\mathbf{R})} (\delta_{\mathbf{R}, \mathbf{R}'} + \delta_{\mathbf{R}+\sqrt{2}a\hat{\gamma}, \mathbf{R}'})$$

and a product term,

$$\begin{aligned} \mathbf{C}_{\mathbf{R}, \mathbf{R}'} &= \frac{K_1 \Delta}{2} \sum_{\hat{\alpha}(\mathbf{R})} \hat{\alpha} (\delta_{\mathbf{R}, \mathbf{R}'} + \delta_{\mathbf{R}+a\hat{\alpha}, \mathbf{R}'}) + \frac{\sqrt{2} K_2 \Delta}{2} \sum_{\hat{\gamma}(\mathbf{R})} \hat{\gamma} (\delta_{\mathbf{R}, \mathbf{R}'} + \delta_{\mathbf{R}+\sqrt{2}a\hat{\gamma}, \mathbf{R}'}) \\ \mathbf{D}_{\mathbf{R}, \mathbf{R}'} &= K_1 \sum_{\hat{\alpha}(\mathbf{R})} \hat{\alpha} \hat{\alpha} (\delta_{\mathbf{R}, \mathbf{R}'} - \delta_{\mathbf{R}+a\hat{\alpha}, \mathbf{R}'}) + K_2 \sum_{\hat{\gamma}(\mathbf{R})} \hat{\gamma} \hat{\gamma} (\delta_{\mathbf{R}, \mathbf{R}'} - \delta_{\mathbf{R}+\sqrt{2}a\hat{\gamma}, \mathbf{R}'}) \end{aligned}$$

requiring the inversion of the matrix $\mathbf{D}_{\mathbf{R}, \mathbf{R}'}$.

2.3. Kinetic Monte Carlo algorithm

For all simulations, the standard Gillespie algorithm⁴⁷ was used to propagate the dynamics. The rate to go from configuration \mathbf{C} to \mathbf{C}' took the form,

$$k_{\mathbf{C}, \mathbf{C}'} = k_0 \exp \left\{ -\frac{\beta}{2} \left(E(\mathbf{C}') - E(\mathbf{C}) \right) + \frac{\beta \Delta \mu}{2} \left((N(\mathbf{C}') - N(\mathbf{C})) \right) \right\} \quad (3)$$

$E(\mathbf{C})$ and $N(\mathbf{C})$ respectively denote the energy and the number of spin up sites in configuration \mathbf{C} . The pre-factor, k_0 , was constant for all processes, and it sets the units of time for the simulation, $k_0^{-1} = \tau_0$. The allowed processes were different for the umbrella sampling and interfacial propagation simulations, which will be described in **Supplementary Notes 2.4, 3.1 and 5.2**.

2.4. Phase diagrams of the model

Supplementary Fig. 9 shows four approximate phase diagrams for nanocubes with side lengths of 10, 15, 20, and 30 sites. At each temperature, at least four independent trajectories were initialized in random configurations with average values of $c_\beta = \sum_{\mathbf{R}} \frac{\sigma_{\mathbf{R}} + 1}{2N}$ of 0.75 and 0.25. The trajectories were propagated for at least 500 rejection-free kinetic Monte Carlo sweeps, and up to 10^4 sweeps in the case of the smaller cubes. The allowed moves were spin flips and nearest neighbor exchanges. The average value of c_β was computed along each trajectory after discarding 200 sweeps for equilibration. The two markers for each temperature in **Supplementary Fig. 9** are the averages across the independent trajectories beginning near $c_\beta = 0.25$ and $c_\beta = 0.75$, respectively. The error bars are three standard errors in the mean across the independent trajectories. The dashed lines are quartic fits to the markers, where the fourth-order coefficient is enforced to be negative.

For a system of infinite extent, one can obtain an analytic form for the interaction potential of **Supplementary Equation 2**, in a Fourier basis.⁴⁸ Using a numerical Fourier transform, we can construct a Hamiltonian of the form,

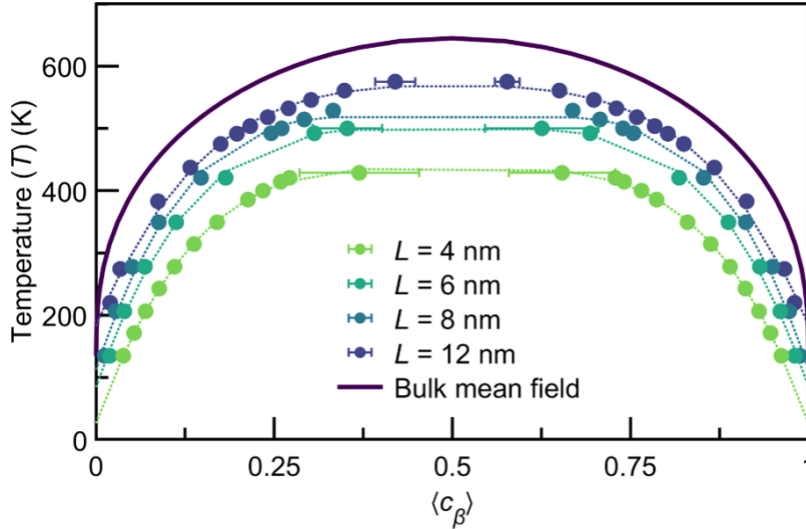
$$H_{\text{eff}} = \frac{1}{2} \sum_{\mathbf{R}, \mathbf{R}' \neq \mathbf{R}} \sigma_{\mathbf{R}} V^{\text{bulk}}(\mathbf{R} - \mathbf{R}') \sigma_{\mathbf{R}'} \quad (4)$$

The simplest mean-field theory for this Hamiltonian yields the self-consistent equation,

$$\tanh(\beta \bar{V} m) = m \quad (5)$$

$$\bar{V} = \sum_{\mathbf{R}' \neq \mathbf{R}} V^{\text{bulk}}(\mathbf{R} - \mathbf{R}'), \quad m = \frac{1}{N} \sum_{\mathbf{R}} \sigma_{\mathbf{R}}$$

Calculating \bar{V} out to 256 lattice sites in all three Cartesian directions, we obtain a bulk, mean-field critical point, $T_c^{\text{MF}} = 644.7\text{K}$. The solid line in **Supplementary Fig. 9** is the numerical solution to **Supplementary Equation 5** with this value of \bar{V} . All simulations are run at 300 K.



Supplementary Fig. 9. Phase diagrams for the elastic Ising model, for different size nanocubes (with side length, L). Markers are averages over at least 4 independent trajectories of lengths of at least 500 rejection-free KMC sweeps. Dashed lines are quartic fits to the markers. The solid line is the numerical solution to an equation of state under a simple mean-field approximation in a bulk system.

3. Free energy calculations

3.1. Computational details

Umbrella sampling calculations were carried out using c_β as the order parameter on cubes of side length, 15 sites or approximately 6 nm. 415 umbrellas were used with centers between $c_\beta^* = -0.05$ and $c_\beta^* = 1.05$. The biasing

potential was of the form $U = KN(c_\beta - c_\beta^*)^2/2$. Three spring constants were used in different ranges of c_β^* , which are summarized in **Supplementary Table 2**. Trajectories were run with kinetic Monte Carlo (KMC) dynamics, with spin flips allowed at the boundary of the nanocube and exchanges allowed between any nearest-neighbor sites. 200 rejection-free sweeps were discarded for equilibration in each trajectory. The correlation time for the concentration was assumed to be less than five rejection-free sweeps in each trajectory. Trajectories were between 5×10^3 and 5×10^4 rejection-free sweeps in length. The weighted histogram analysis method (WHAM)⁴⁹ was used to construct the free energy profile with a tolerance of 10^{-3} . To estimate the statistical error, trajectories were split into five segments of equal length, and separate WHAM calculations were performed on each data set. Three standard errors in the mean of the five independent calculations are smaller than the line widths of **Extended Data Fig. 2a,b**.

c_β^* range	Spring constant (eV)
-0.05 to 0.09	0.8402
0.10 to 0.40	0.6463
0.40 to 0.60	0.4524
0.60 to 0.90	0.6463
0.90 to 1.05	0.8402

Supplementary Table 2: Spring constants used for umbrella sampling for umbrellas with centers in different ranges.

3.2. The energetics of idealized configurations

To further understand the observed absorption pathway, we studied the elastic energies of **Supplementary Equation 2** from idealized configurations along potential pathways of absorption. We consider perfect interfaces in the $\langle 100 \rangle$, $\langle 110 \rangle$, and $\langle 111 \rangle$ directions moving across the cube. In **Extended Data Fig. 3**, we compute the energies for different size nanocubes for each of the interfaces. We observe that the energetic cost to form any interface scales extensively, and that for each of the sizes the $\langle 100 \rangle$ interface is significantly energetically preferred near $c_\beta = 0.5$. However, for c_β below 0.25, the most energetically preferred interface is along the $\langle 110 \rangle$ direction, corresponding to the corner-nucleus configurations observed in both the model and in the experiment. Thus, it seems the observed absorption pathway can be understood mainly in terms of minimizing the cost in elastic energy due to the interface between the two phases at each value of c_β . In addition, the energetic cost to form any interface increases in proportion to system size, while the differences in the energetics among the $\langle 100 \rangle$, $\langle 110 \rangle$, and $\langle 111 \rangle$ directions remain constant. Therefore, we can expect that the reversible pathway observed in **Extended Data Fig. 2** will be consistent as the nanocube approaches the size used in the liquid phase TEM experiments.

4. Theoretical simulation of hydrogen absorption pathway in palladium nanocubes

Simulations of hydrogen absorption and desorption are conducted with kinetic Monte Carlo of the elastic Ising model Hamiltonian³³⁻³⁵ (see **Supplementary Note 2.1-2.3**). The elastic Ising model accounts for the energetic cost of the strain that is induced due to the difference in lattice constants between regions of the nanocube rich in α -PdH_x and those rich in β -PdH_x. In the model, a nanocube is coarse-grained such that each unit cell is defined to be either α -PdH_x or β -PdH_x phase, and the Hamiltonian is parameterized with experimental values of the elastic moduli of PdH_x⁴⁵ (see **Supplementary Note 2.1**) in order to describe the elastic mediated effective interaction potential between each site. **Supplementary Fig. 9** shows that with this parameterization, the simple model exhibits a phase diagram that is quantitatively similar to the experimental diagram in the bulk⁵⁰ (see **Supplementary Note 2.4**). It also captures the expected effects of nanoscale confinement, in a suppressed critical temperature and enhanced equilibrium concentration of hydrogen at the interface in the α -PdH_x phase for smaller cubes.¹⁷

To investigate the pathways of reversible absorption in the model, free energy calculations are carried out as a function of the concentration of β -PdH_x (c_β) at coexistence (**Extended Data Fig. 2a**) and away from it (**Extended Data Fig. 2b**), using umbrella sampling (see **Supplementary Note 3.1**). Representative configurations from four points along the absorption pathway (**Extended Data Fig. 2c,d** and **Supplementary Video 2**) recapitulate the observed experimental pathway of nucleation at one corner followed by propagation of the interface along a $\langle 100 \rangle$ direction. **Extended Data Fig. 2e** shows that the corner nucleated configuration contains an interface, approximately in a $\langle 110 \rangle$ direction, that spans the length of the cube. This interface then moves in either of the two equivalent $\langle 100 \rangle$ directions, in order to join with an opposite face of the cube and form a stable $\{100\}$ interface that spans the cube. **Extended Data Fig. 2b** depicts the shift in the free energy curve **Extended Data Fig. 2a** in response to a chemical potential difference, $\Delta\mu$, between the H₂ molecules in solution and the H atoms in the palladium lattice, which would act as a chemical driving force for absorption. The curves show that the single-corner configuration represents a critical nucleus when the chemical driving force is significantly smaller than the thermal

energy. While free energy curves are only presented for an approximately 6 nm cube due to computational limitations, we expect that the reversible absorption pathway would be recapitulated in larger cubes, as is observed in the liquid phase TEM (see **Supplementary Note 3.2**). Additionally, the model includes neither effects from diffusion of H₂ in solution nor defects in the nanocube. This indicates that the corner nucleation and [100] propagation pathway can be understood purely in terms of the energetics of elastic interactions (see **Supplementary Note 3.2**). The free energy curves have only a single barrier, meaning that the stagnation in the reaction observed experimentally after the corner nucleation (see **Supplementary Note 1 and Extended Data Fig. 1c**) is likely due to either a depletion of H₂ concentration near the cube, or the need to overcome an energetic barrier caused by a defect.

5. Interfacial propagation simulations

5.1. Construction of density field and interface

A configuration in the elastic Ising model is represented by a discrete spin-field, where each site has a value of ± 1 . However, in the physical system, hydrogen density should vary continuously over space. To produce the density maps of **Extended Data Fig. 2c-e** and **Fig. 4a,b**, we used the procedure of Willard and Chandler,⁵¹ convoluting the discrete density field with Gaussian distributions, such that the density for a given site is equal to,

$$\tilde{c}_\beta(\mathbf{R}) = \frac{1}{\mathcal{N}} \sum_{\mathbf{R}'} \sigma_{\mathbf{R}'} e^{-\frac{|\mathbf{R}' - \mathbf{R}|^2}{2a^2}} \quad (6)$$

In **Supplementary Equation 6**, a , is the lattice constant of the model. In practice, the sum was cut off at a distance of five unit cells, and \mathcal{N} is the normalization of the discretized Gaussian over this range. Periodic boundary conditions were used in the x and y directions, to compute the density field for the rod geometries. For the cube geometries of **Extended Data Fig. 2c-e**, and for the z -direction of the rod geometries, hard-wall boundaries are used. This means that, in **Supplementary Equation 6**, $\sigma_{\mathbf{R}} = 0$ if \mathbf{R} is outside the nanocrystal.

This convoluted density field was also used to compute the field, $h(x, y)$, that defines the interface in the simulations of interfacial propagation (**Fig. 4**). For each pair of x and y values defining a column of sites along the z -axis, the z -value, z^* , was identified such that $z^*(x, y) = \min\{z \mid \tilde{c}_\beta(x, y, z) < 0.5\}$. Then, via linear interpolation between $\tilde{c}_\beta(x, y, z^* - a)$ and $\tilde{c}_\beta(x, y, z^*)$, the value of $h(x, y)$ was determined such that $\tilde{c}_\beta(x, y, h(x, y)) = 0.5$. We then define the position of the interface at a time, t , in **Supplementary Equation 7**.

$$\frac{\bar{h}(t)}{a} = \frac{1}{N_{xy}} \sum_{x,y} h(x, y, t) \quad (7)$$

Here, N_{xy} is the number of total unit cells in the x and y dimensions, or number of columns.

We also define the instantaneous width of the interface in **Supplementary Equation 8**,

$$(\delta h)^2/a^2 = \frac{1}{N_{xy}} \sum_{x,y} \left(h(x, y, t) - \bar{h}(t) \right)^2 \quad (8)$$

as the variance of the height field. And, lastly, we define the average velocity of the interface over a given time period in **Supplementary Equation 9**.

$$\bar{v} = \frac{\bar{h}(t_b) - \bar{h}(t_a)}{t_b - t_a} \quad (9)$$

To compute the velocities in **Fig. 4** and **Extended Data Fig. 4**, t_b and t_a were taken to be the time when \bar{h} reached $25a$ and $31a$, respectively, for each independent trajectory.

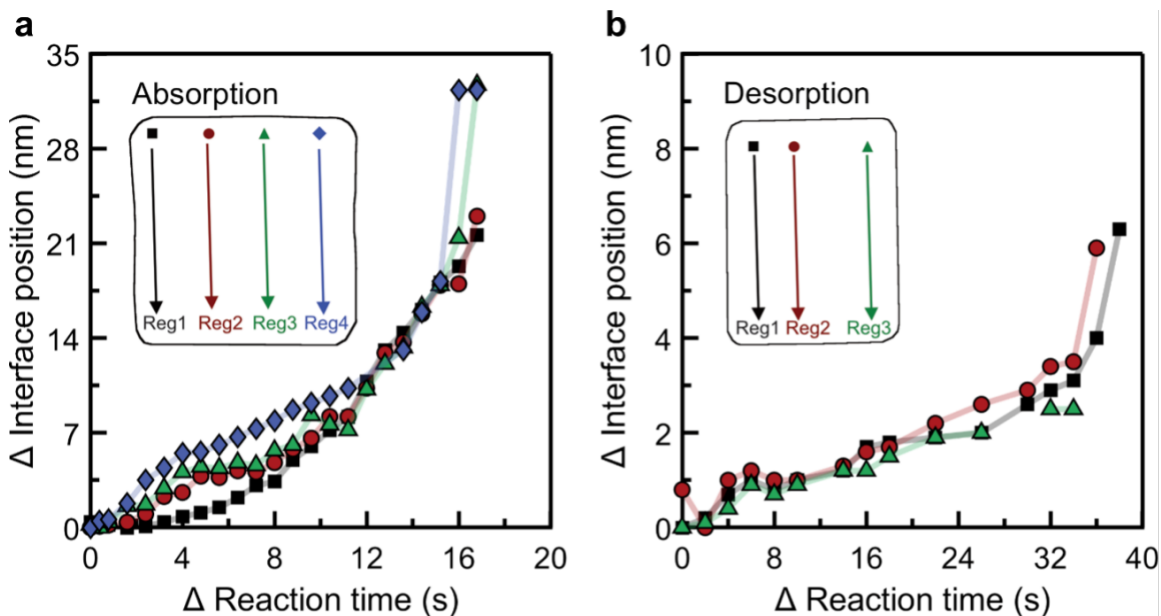
5.2. Computational details of rod trajectories

To decouple the nucleation process from the interfacial dynamics, the simulations of interfacial propagation of **Fig. 4** were carried out with constrained dynamics in a rod geometry of $16 \times 16 \times 50$ unit cells. Propagation of β -PdH_x was directed in the positive z -direction by holding the spins at the $z/a = 1$ layer of the rod fixed at ± 1 and the spins at the $z/a = 50$ layer of the rod fixed as -1 . Due to computational constraints, the size of the rod in the x and y dimensions is significantly smaller than the nanocube used in the experiment. However, with our constrained dynamics, the rod can be seen as the core of a larger nanocube (**Extended Data Fig. 4a**). We allow the exchange of

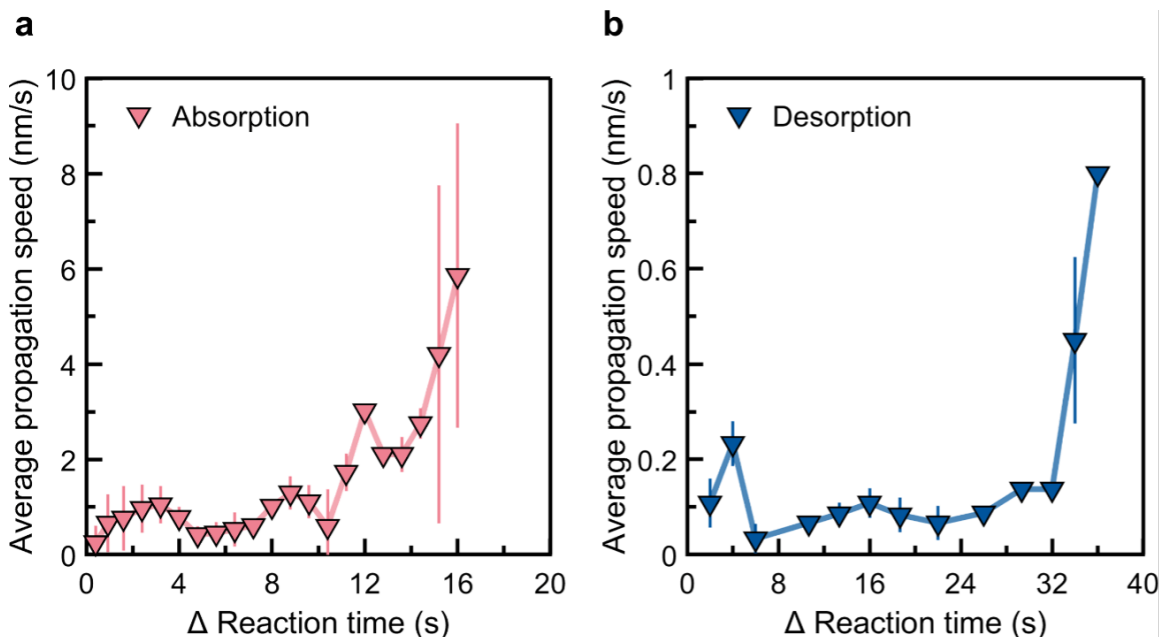
spins between any two nearest neighbors, and we allow any single spin to be flipped if it is a site at an interface, which is defined as any site that has both spin up and spin down nearest neighbors. This is representative of the dynamics in the larger nanocube in which hydrogen is absorbed at the surface of the nanocube and then preferentially diffuses along the interface, towards the core of the cube. It is consistent with the well-separated phase domains observed in the liquid phase TEM experiments.

To verify that the observed behavior of interfacial propagation remains qualitatively consistent across different sizes of the rod geometry, we ran simulations with rods of sizes 12, 14, and 16 unit cells in the x - y dimensions, keeping the length in the z -dimension fixed at 50 unit cells. At low chemical driving force, $\Delta\mu < 0.5 k_B T$, there is no statistically significant dependence of the average interfacial width or average velocity on the size in the x - y dimensions, for the sizes we have tested (**Extended Data Fig. 4b-d**). Under a large chemical driving force, $\Delta\mu > 0.5 k_B T$, the interfacial width does acquire a non-trivial dependence on the size of the x - y dimensions. Under these conditions, the interfacial width diverges over time, and the rate of this divergence appears to depend on the width of the rod, as would be expected from a general, theoretical description of kinetic roughening.⁴⁰ In all such cases, there is a clear distinction between a smooth regime, in which the interfacial width is constant over time, and a kinetically rough regime, in which the interfacial width increases over time (**Extended Data Fig. 4d**). Additionally, the relative increase in the speed of propagation under a large chemical driving force, $\Delta\mu > 0.5 k_B T$, decreases slightly with the increasing width of the rod. However, extrapolating the trend from 12 to 14 to 16 unit cells in rod-width (**Extended Data Fig. 4c**), it appears that the speed will converge as the size increases and that the relative increase in propagation speed will remain of the same order of magnitude as the difference in propagation speed between absorption and desorption observed in the liquid phase TEM. Therefore, the qualitative conclusion that kinetic roughening contributes to the expanding of the interface observed during faster propagation in the liquid phase TEM experiments remains valid.

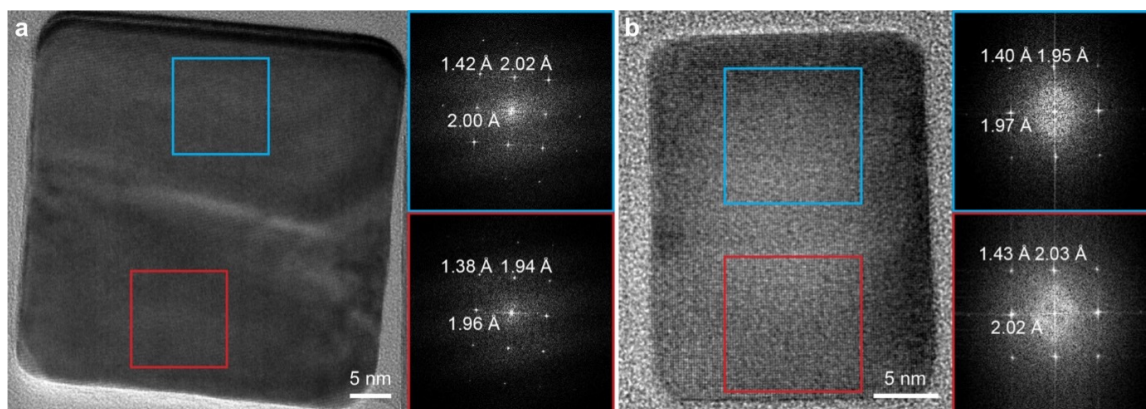
To compute average quantities like the velocity and the interfacial width, data was taken from at least 115 independent trajectories under each value of $\Delta\mu$. Every trajectory starts from the same initial condition, which is an entirely spin down (-1) rod, except for the fixed layer of spin up ($+1$) at one end. For the plots in **Fig. 4d,e** and **Extended Data Fig. 4b,c**, an average is first taken for each individual trajectory over the range of time from which the trajectory first reaches $\bar{h}/a = 25$ to the time when it reaches $\bar{h}/a = 31$. This range was chosen such that it was large enough to decrease the sampling error, but small enough so that the interface would not feel effects from the boundaries at the ends of the rods. The time-averages from each of the trajectories are themselves, then further averaged across multiple independent trajectories. Error bars show two standard errors in the mean from the independent trajectories. To compute the time series plots in **Fig. 4c** and **Extended Data Fig. 4d**, a histogram in time is made for each trajectory, and the average value of the observable is computed in each time window. The elapsed time, Δt , is recorded from the time the interface reaches an average height of $\bar{h}/a = 10$. The histograms for each trajectory are then averaged to produce the solid lines. The shaded region of **Extended Data Fig. 4d** represents two standard errors.



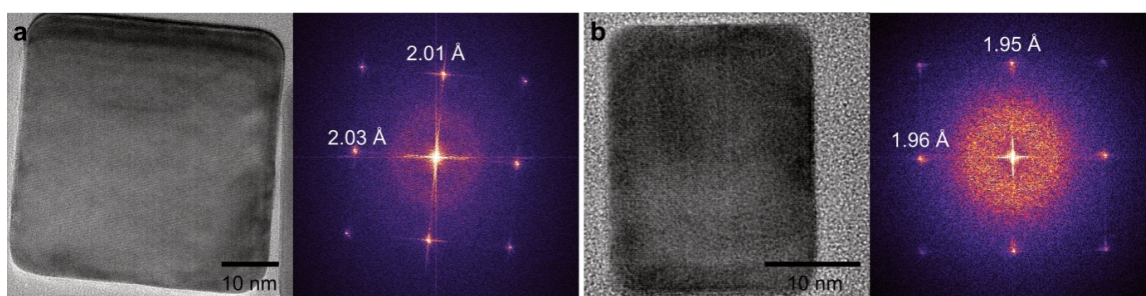
Supplementary Fig. 10. Interface position as a function of time during the hydrogen absorption and desorption reactions. **a,b**, Plots illustrating the interface position along the [100] direction with reaction time during the absorption (**a**) and desorption (**b**) reactions. As illustrated in the inset images, four and three different interface regions ('Regs') were analyzed for the absorption and desorption cases, respectively. Please note that the speed of interface movement notably differs at the different Regs for the absorption case.



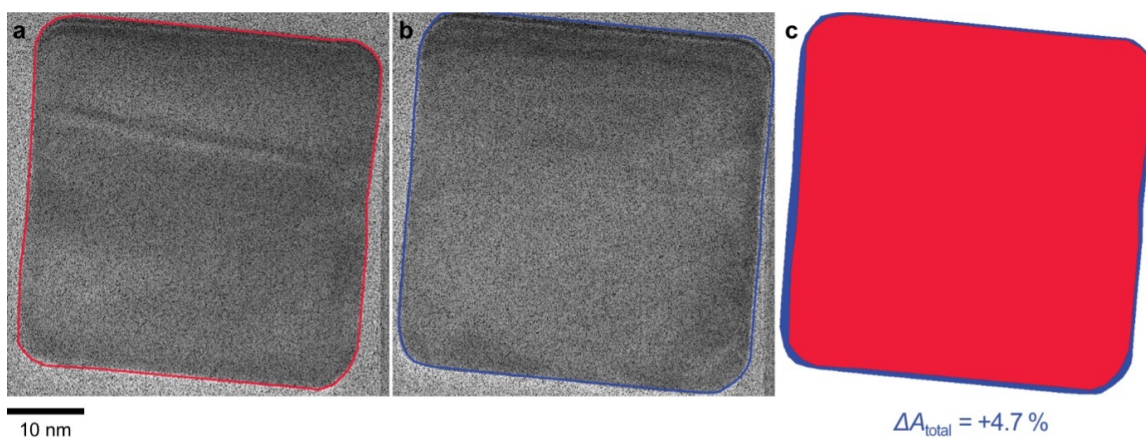
Supplementary Fig. 11. Comprehensive analysis of phase propagation speeds during the absorption and desorption. **a,b**, Graphs depicting the average speed of interface movement (*i.e.*, phase propagation) along the [100] direction as a function of reaction time observed during the absorption (**a**) and desorption (**b**) processes. The propagation speed as a function of time was calculated using a linear fit applied to three consecutive data points from **Supplementary Fig. 10**. Subsequently, these calculated speeds were averaged across all regions to provide a comprehensive view of the phase propagation dynamics for both absorption and desorption. Error bars display standard deviations.



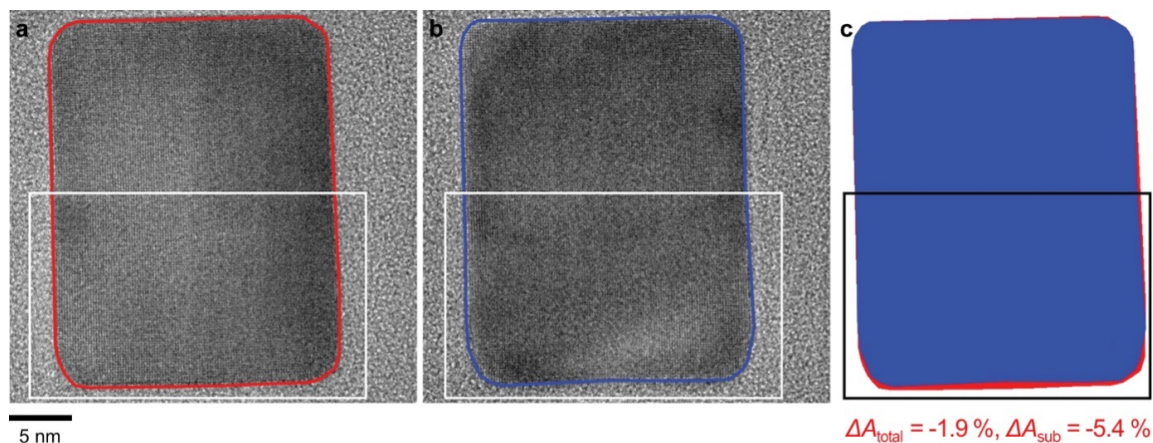
Supplementary Fig. 12. Co-existence of two PdH_x phases in the Pd nanocubes during the hydrogen absorption and desorption. **a,b**, HRTEM images of the nanocubes in the middle of the hydrogen absorption (**a**) and desorption (**b**) reactions. These images are from **Supplementary Videos 3 and 4**. The corresponding FFT patterns from the selected regions (colored rectangles) within the nanocubes are also displayed along with the assigned *d*-spacing values, demonstrating the co-existence of both α - and β -PdH_x phases.



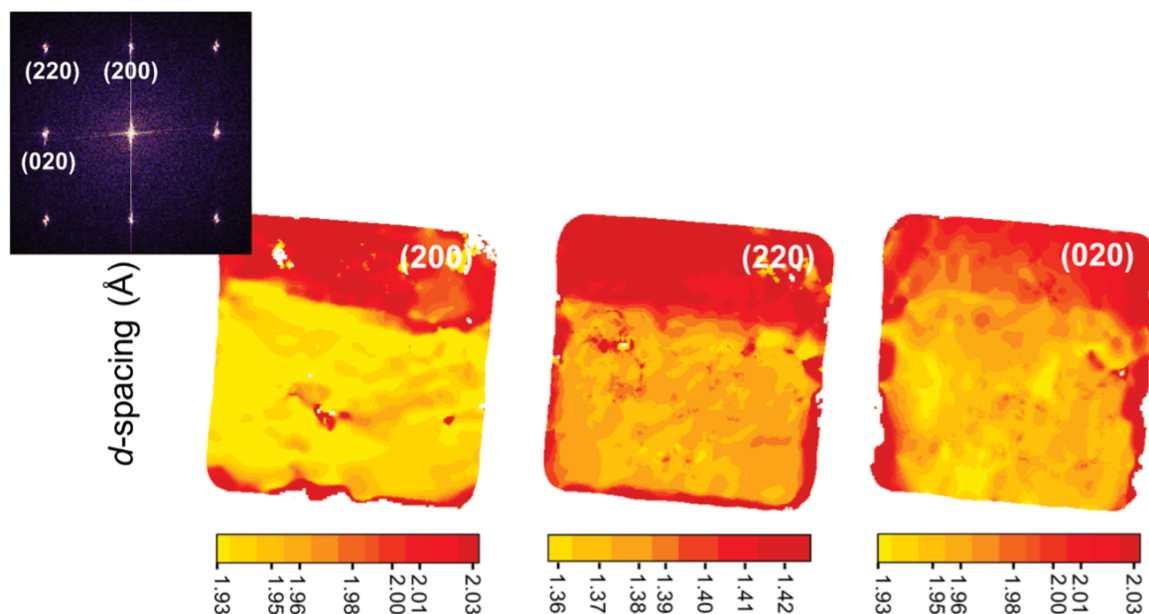
Supplementary Fig. 13. Complete transformation into single-crystalline α - or β -PdH_x phases after the absorption and desorption reactions. **a,b**, HRTEM images of the nanocubes after the hydrogen absorption (**a**) and desorption (**b**). These images are from **Supplementary Videos 3 and 4**. The corresponding FFT patterns from the entire nanocubes are presented with the respective *d*-spacing values, showing the complete phase transformations into α - or β -PdH_x phases. The nanocubes are single-crystalline after the hydrogen absorption and desorption reactions.



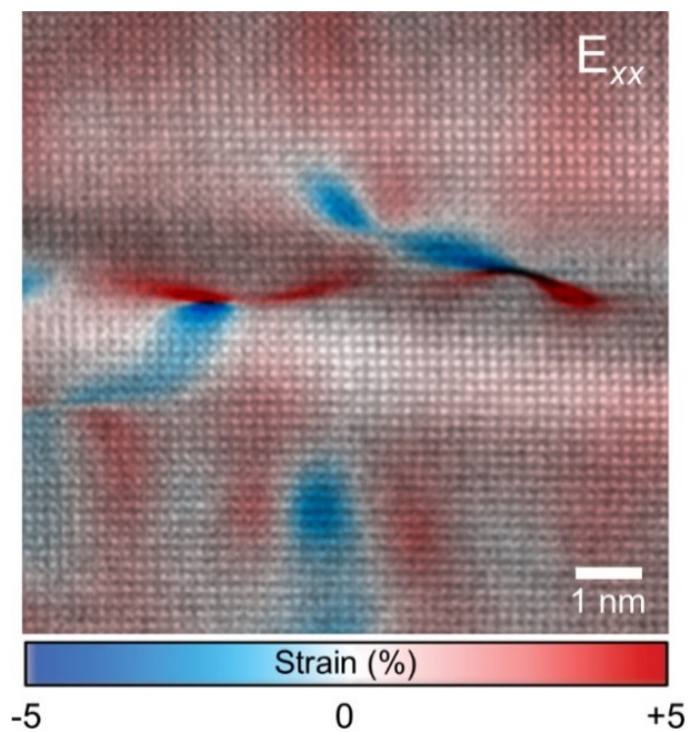
Supplementary Fig. 14. Swelling of the palladium nanocube due to hydrogen absorption. **a,b,c**, This figure compares the 2D projected area of the palladium nanocube at the start of the recorded absorption process (**a**) with its area after complete phase transformation (**b**). The transformation results in a 4.7% increase in the projected area (**c**).



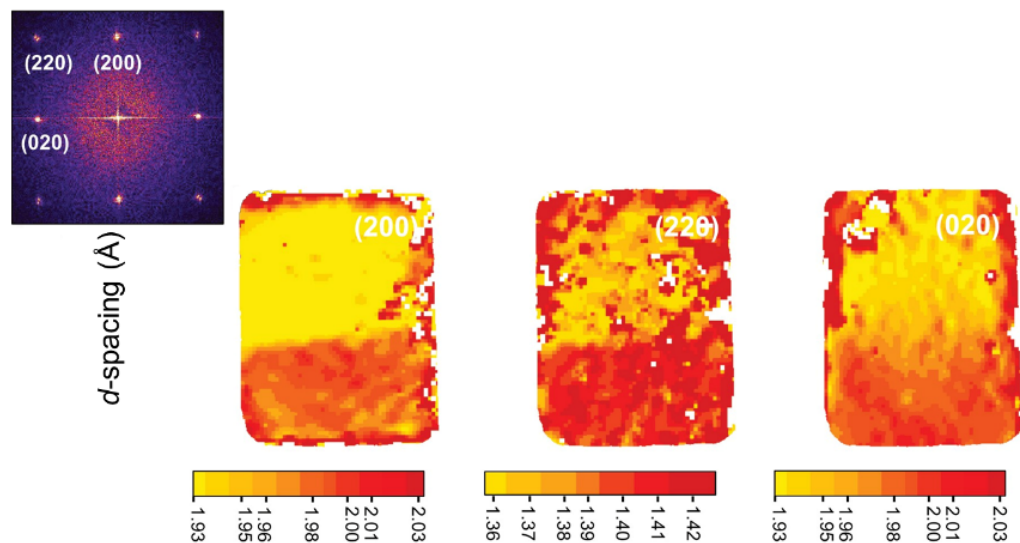
Supplementary Fig. 15. Shrinking of the palladium nanocube due to hydrogen desorption. **a,b,c**, This figure illustrates the change in the 2D projected area of the palladium nanocube at the onset of the imaged desorption process (**a**) and after complete phase transformation (**b**). Overall, there is a 1.9% reduction in the nanocube's projected area. However, since only 50% of the nanocube is β -PdH_x at the start of the HRTEM imaging (**a**), a more precise comparison involves only the β -PdH_x portion (marked by white rectangles in (**a**) and (**b**), and a black rectangle in (**c**)), showing a 5.4% decrease in this specific area (**c**).



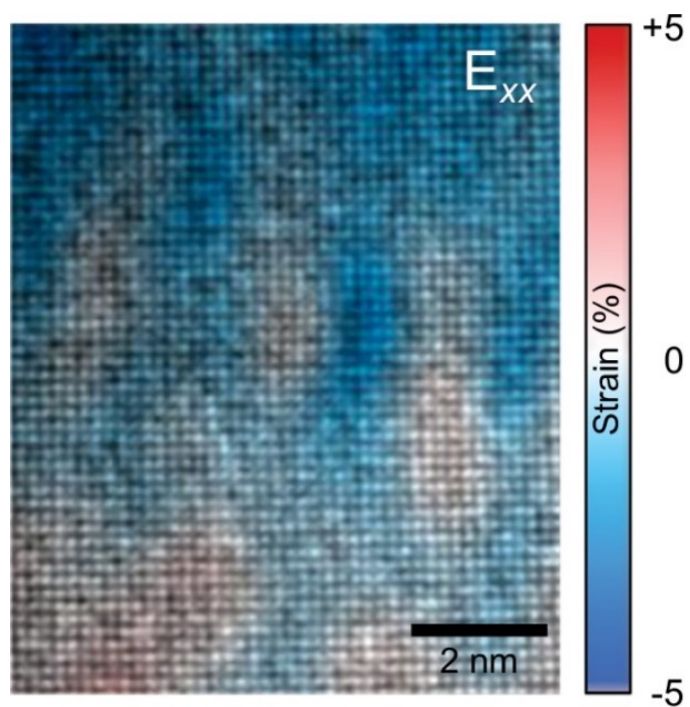
Supplementary Fig. 16. Local variations in d -spacing values in terms of various Bragg reflections from the nanocube during the absorption. The d -spacing color maps from the (200), (220), and (020) reflections (represented in the FFT pattern) of the Pd nanocube during the absorption reaction. Please note that the (200) color map is the same as **Fig. 2b**.



Supplementary Fig. 17. GPA E_{xx} strain map overlaid on the HRTEM image. GPA analysis performed on the [010] (E_{xx}) direction related to the E_{yy} strain map in **Fig. 2d**. No significant strain variations at the interphase boundary are visible in the [010] direction.



Supplementary Fig. 18. Local variations in d -spacing values in terms of various Bragg reflections from the nanocube during the desorption. The d -spacing color maps from the (200), (220), and (020) reflections (represented in the FFT pattern) of the Pd nanocube during the desorption reaction. Please note that the (200) color map is the same as **Fig. 3b**.



Supplementary Fig. 19 GPA E_{xx} strain map overlaid on the HRTEM image. GPA analysis at the interface, which corresponds to the E_{yy} strain map in **Fig. 3c**, demonstrates a relatively smooth strain variation in the [010] (E_{xx}) direction.

References

- ¹H. Zhang, N. Pryds, D.-S. Park, N. Gauquelin, S. Santucci, D. V. Christensen, D. Jannis, D. Chezganov, D. A. Rata, A. R. Insinga, I. E. Castelli, J. Verbeeck, I. Lubomirsky, P. Muralt, D. Damjanovic, and V. Esposito, "Atomically engineered interfaces yield extraordinary electrostriction," *Nature* **609** (2022).
- ²X. Sun, D. Wu, L. Zou, S. D. House, X. Chen, M. Li, D. N. Zakharov, J. C. Yang, and G. Zhou, "Dislocation-induced stop-and-go kinetics of interfacial transformations," *Nature* **607** (2022).
- ³H. Zheng, J. Wang, S. E. Lofland, Z. Ma, L. Mohaddes-Ardabili, T. Zhao, L. Salamanca-Riba, S. R. Shinde, S. B. Ogale, F. Bai, D. Viehland, Y. Jia, D. G. Schlom, M. Wuttig, A. Roytburd, and R. Ramesh, "Multiferroic BaTiO₃-CoFe₂O₄ Nanostructures," *Science* **303** (2004).
- ⁴A. Baldi, T. C. Narayan, A. L. Koh, and J. A. Dionne, "In situ detection of hydrogen-induced phase transitions in individual palladium nanocrystals," *Nature Mater* **13** (2014).
- ⁵L. Zou, C. Yang, Y. Lei, D. Zakharov, J. M. K. Wiezorek, D. Su, Q. Yin, J. Li, Z. Liu, E. A. Stach, J. C. Yang, L. Qi, G. Wang, and G. Zhou, "Dislocation nucleation facilitated by atomic segregation," *Nature Mater* **17**, 56–63 (2018).
- ⁶S. Syrenova, C. Wadell, F. A. A. Nugroho, T. A. Gschneidner, Y. A. Diaz Fernandez, G. Nalin, D. Świtlik, F. Westerlund, T. J. Antosiewicz, V. P. Zhdanov, K. Moth-Poulsen, and C. Langhammer, "Hydride formation thermodynamics and hysteresis in individual Pd nanocrystals with different size and shape," *Nature Mater* **14**, 1236–1244 (2015).
- ⁷J. A. Steele, H. Jin, I. Dovgaliuk, R. F. Berger, T. Braeckvelt, H. Yuan, C. Martin, E. Solano, K. Lejaeghere, S. M. J. Rogge, C. NOOPnotebaert, W. Vandezande, K. P. F. Janssen, B. Goderis, E. Debroye, Y.-K. Wang, Y. Dong, D. Ma, M. Saidaminov, H. Tan, Z. Lu, V. Dyadkin, D. Chernyshov, V. Van Speybroeck, E. H. Sargent, J. Hofkens, and M. B. J. Roeffaers, "Thermal nonequilibrium of strained black CsPbI₃ thin films," *Science* **365**, 679–684 (2019).
- ⁸Y. Chen, Y. Lei, Y. Li, Y. Yu, J. Cai, M.-H. Chiu, R. Rao, Y. Gu, C. Wang, W. Choi, H. Hu, C. Wang, Y. Li, J. Song, J. Zhang, B. Qi, M. Lin, Z. Zhang, A. E. Islam, B. Maruyama, S. Dayeh, L.-J. Li, K. Yang, Y.-H. Lo, and S. Xu, "Strain engineering and epitaxial stabilization of halide perovskites," *Nature* **577**, 209–215 (2020).
- ⁹G. Liu, A. J. Shih, H. Deng, K. Ojha, X. Chen, M. Luo, I. T. McCrum, M. T. M. Koper, J. Greeley, and Z. Zeng, "Site-specific reactivity of stepped Pt surfaces driven by stress release," *Nature* **626**, 1005–1010 (2024).
- ¹⁰Z. Bai, A. Misra, and Y. Fan, "Universal Trend in the dynamic relaxations of tilted metastable grain boundaries during ultrafast thermal cycle," *Materials Research Letters* **10**, 343–351 (2022).
- ¹¹M. H. Oh, M. G. Cho, D. Y. Chung, I. Park, Y. P. Kwon, C. Ophus, D. Kim, M. G. Kim, B. Jeong, X. W. Gu, J. Jo, J. M. Yoo, J. Hong, S. McMains, K. Kang, Y.-E. Sung, A. P. Alivisatos, and T. Hyeon, "Design and synthesis of multigrain nanocrystals via geometric misfit strain," *Nature* **577**, 359–363 (2020).
- ¹²Y. Xu, J.-H. Park, Z. Yao, C. Wolverton, M. Razeghi, J. Wu, and V. P. Dravid, "Strain-Induced Metastable Phase Stabilization in Ga₂O₃ Thin Films | ACS Applied Materials & Interfaces," (2019).
- ¹³J. Kacher, B. P. Eftink, and I. M. Robertson, "In situ transmission electron microscopy investigation of dislocation interactions," in *Handbook of Mechanics of Materials* (Unknown Publisher, 2019) pp. 131–166.
- ¹⁴R. W. G. Wyckoff, *The Structure of Crystals* (Chemical Catalog Company, Incorporated, 1924).
- ¹⁵E. Wicke and H. Brodowsky, "Hydrogen in palladium and palladium alloys," , 73–155 (1978).
- ¹⁶B. Ingham, M. F. Toney, S. C. Hendy, T. Cox, D. D. Fong, J. A. Eastman, P. H. Fuoss, K. J. Stevens, A. Lassesson, S. A. Brown, and M. P. Ryan, "Particle size effect of hydrogen-induced lattice expansion of palladium nanoclusters," *Phys. Rev. B* **78**, 245408 (2008).
- ¹⁷M. Yamauchi, R. Ikeda, H. Kitagawa, and M. Takata, "Nanosize Effects on Hydrogen Storage in Palladium," *J. Phys. Chem. C* **112**, 3294–3299 (2008).
- ¹⁸N. Liu, M. L. Tang, M. Hentschel, H. Giessen, and A. P. Alivisatos, "Nanoantenna-enhanced gas sensing in a single tailored nanofocus," *Nature Mater* **10**, 631–636 (2011).
- ¹⁹R. Bardhan, L. O. Hedges, C. L. Pint, A. Javey, S. Whitelam, and J. J. Urban, "Uncovering the intrinsic size dependence of hydriding phase transformations in nanocrystals," *Nature Mater* **12**, 905–912 (2013).
- ²⁰G. Li, H. Kobayashi, J. M. Taylor, R. Ikeda, Y. Kubota, K. Kato, M. Takata, T. Yamamoto, S. Toh, S. Matsumura, and H. Kitagawa, "Hydrogen storage in Pd nanocrystals covered with a metal–organic framework," *Nature Mater* **13**, 802–806 (2014).
- ²¹R. Griessen, N. Strohheldt, and H. Giessen, "Thermodynamics of the hybrid interaction of hydrogen with palladium nanoparticles," *Nature Mater* **15**, 311–317 (2016).
- ²²T. C. Narayan, F. Hayee, A. Baldi, A. Leen Koh, R. Sinclair, and J. A. Dionne, "Direct visualization of hydrogen absorption dynamics in individual palladium nanoparticles," *Nat Commun* **8**, 14020 (2017).
- ²³A. Ulvestad, M. J. Welland, W. Cha, Y. Liu, J. W. Kim, R. Harder, E. Maxey, J. N. Clark, M. J. Highland, H. You, P. Zapol, S. O. Hruszkewycz, and G. B. Stephenson, "Three-dimensional imaging of dislocation dynamics during the hydriding phase transformation," *Nature Mater* **16**, 565–571 (2017).
- ²⁴A. Schneemann, J. L. White, S. Kang, S. Jeong, L. F. Wan, E. S. Cho, T. W. Heo, D. Prendergast, J. L. Urban, B. C. Wood, M. D. Allendorf, and V. Stavila, "Nanostructured Metal Hydrides for Hydrogen Storage | Chemical Reviews," (2018).
- ²⁵K. Sytzu, F. Hayee, T. C. Narayan, A. L. Koh, R. Sinclair, and J. A. Dionne, "Visualizing Facet-Dependent Hydrogenation Dynamics in Individual Palladium Nanoparticles," *Nano Lett.* **18**, 5357–5363 (2018).
- ²⁶N. J. J. Johnson, B. Lam, B. P. MacLeod, R. S. Sherbo, M. Moreno-Gonzalez, D. K. Fork, and C. P. Berlinguette, "Facets and vertices regulate hydrogen uptake and release in palladium nanocrystals," *Nat. Mater.* **18**, 454–458 (2019).
- ²⁷K. Koo, Z. Li, Y. Liu, S. M. Ribet, X. Fu, Y. Jia, X. Chen, G. Shekawat, P. J. M. Smeets, R. dos Reis, J. Park, J. M. Yuk, X. Hu, and V. P. Dravid, "Ulathin silicon nitride microchip for in situ/operando microscopy with high spatial resolution and spectral visibility," *Science Advances* **10**, eadj6417 (2024).
- ²⁸Z.-W. Yin, S. B. Betzler, T. Sheng, Q. Zhang, X. Peng, J. Shang-guan, K. C. Bustillo, J.-T. Li, S.-G. Sun, and H. Zheng, "Visualization of facet-dependent pseudo-photocatalytic behavior of TiO₂ nanorods for water splitting using In situ liquid cell TEM," *Nano Energy* **62**, 507–512 (2019).
- ²⁹Q. Zhang, X. Peng, Y. Nie, Q. Zheng, J. Shangguan, C. Zhu, K. C. Bustillo, P. Ercius, L. Wang, D. T. Limmer, and H. Zheng, "Defect-mediated ripening of core-shell nanostructures," *Nat Commun* **13**, 2211 (2022).
- ³⁰E. J. Hart, "The Hydrated Electron," *Science* **146**, 19–25 (1964).
- ³¹J. M. Grogan, N. M. Schneider, F. M. Ross, and H. H. Bau, "Bubble and Pattern Formation in Liquid Induced by an Electron Beam," *Nano Lett.* **14**, 359–364 (2014).
- ³²N. M. Schneider, M. M. Norton, B. J. Mendel, J. M. Grogan, F. M. Ross, and H. H. Bau, "Electron–Water Interactions and Implications for Liquid Cell Electron Microscopy | The Journal of Physical Chemistry C," (2014).
- ³³P. Fratzl, O. Penrose, and J. L. Lebowitz, "Modeling of Phase Separation in Alloys with Coherent Elastic Misfit," *Journal of Statistical Physics* **95**, 1429–1503 (1999).
- ³⁴L. B. Frechette, C. Dellago, and P. L. Geissler, "Origin of mean-field behavior in an elastic Ising model," *Phys. Rev. B* **102**, 024102 (2020).
- ³⁵L. B. Frechette, C. Dellago, and P. L. Geissler, "Elastic forces

- drive nonequilibrium pattern formation in a model of nanocrystal ion exchange | PNAS,” (2021).
- ³⁶M. J. Hÿtch, E. Snoeck, and R. Kilaas, “Quantitative measurement of displacement and strain fields from HREM micrographs,” *Ultramicroscopy* **74**, 131–146 (1998).
- ³⁷J. L. Rouvière and E. Sarigiannidou, “Theoretical discussions on the geometrical phase analysis,” *Ultramicroscopy* **106**, 1–17 (2005).
- ³⁸Y. Zhu, C. Ophus, J. Ciston, and H. Wang, “Interface lattice displacement measurement to 1 nm by geometric phase analysis on aberration-corrected HAADF STEM images,” *Acta Materialia* **61**, 5646–5663 (2013).
- ³⁹M. Nishino, T. Nakada, C. Enachescu, K. Boukheddaden, and S. Miyashita, “Crossover of the roughness exponent for interface growth in systems with long-range interactions due to lattice distortion,” (2013).
- ⁴⁰W. M. Tong and R. S. Williams, “Kinetics of Surface Growth: Phenomenology, Scaling, and Mechanisms of Smoothing and Roughening,” *Annual Review of Physical Chemistry* **45**, 401–438 (1994).
- ⁴¹S. Mukherji and S. M. Bhattacharjee, “Nonlocality in Kinetic Roughening,” *Phys. Rev. Lett.* **79**, 2502–2505 (1997).
- ⁴²P. S. Epstein and M. S. Plesset, “On the Stability of Gas Bubbles in Liquid-Gas Solutions,” *The Journal of Chemical Physics* **18**, 1505–1509 (1950).
- ⁴³Q. Kim, D. Shin, J. Park, D. A. Weitz, and W. Jhe, “Initial growth dynamics of 10 nm nanobubbles in the graphene liquid cell,” *Appl Nanosci* **11**, 1–7 (2021).
- ⁴⁴B. R. Jany, A. Janas, and F. Krok, “Automatic microscopic image analysis by moving window local Fourier Transform and Machine Learning,” *Micron* **130**, 102800 (2020).
- ⁴⁵D. K. Hsu and R. G. Leisure, “Elastic constants of palladium and β -phase palladium hydride between 4 and 300 K,” *Phys. Rev. B* **20**, 1339–1344 (1979).
- ⁴⁶L. B. Frechette, C. Dellago, and P. L. Geissler, “Consequences of Lattice Mismatch for Phase Equilibrium in Heterostructured Solids,” *Phys. Rev. Lett.* **123**, 135701 (2019).
- ⁴⁷D. T. Gillespie, “Stochastic Simulation of Chemical Kinetics,” *Annual Review of Physical Chemistry* **58**, 35–55 (2007).
- ⁴⁸L. B. Frechette, *Chemical Transformations of Nanocrystals: Theory and Molecular Simulation*, Ph.D., University of California, Berkeley, United States – California (2020).
- ⁴⁹A. Grossfield, “An implementation of WHAM: the Weighted Histogram Analysis Method Version 2.0.10,” (2011).
- ⁵⁰T. B. Flanagan and W. A. Oates, “The Palladium-Hydrogen System,” *Annual Review of Materials Research* **21**, 269–304 (1991).
- ⁵¹A. P. Willard and D. Chandler, “Instantaneous Liquid Interfaces,” *J. Phys. Chem. B* **114**, 1954–1958 (2010).